



GEORG-AUGUST-UNIVERSITÄT  
GÖTTINGEN

---

**Magneto-Seebeck effect in magnetic  
tunnel junctions on MgO substrate**

**Magneto-Seebeck-Effekt in magnetischen  
Tunnelementen auf MgO-Substrat**

---

Bachelor thesis

prepared by

Niklas Roschewsky

from

Jever

at the

Georg-August-Universität Göttingen

I. Physikalisches Institut

2012

**Supervisor:** Marvin Walter  
**First referee:** Prof. Dr. Markus Münzenberg  
**Second referee:** Prof. Dr. Claus Ropers  
**Thesis period:** 25 April 2012 until 01 August 2012

# Contents

<b>1. Introduction</b>	<b>1</b>
<b>2. Theoretical background</b>	<b>3</b>
2.1. Tunnel Effect in the Simmons model . . . . .	3
2.2. Tunneling magneto resistance . . . . .	5
2.2.1. The Julliere model . . . . .	5
2.2.2. Model by Butler et al. . . . .	6
2.3. Classical Seebeck Effect . . . . .	8
2.4. Magneto-Seebeck effect . . . . .	11
<b>3. Experimental setup</b>	<b>15</b>
3.1. Lock-In Amplifier . . . . .	15
3.1.1. General Principle . . . . .	15
3.1.2. Measured Signal . . . . .	17
3.1.3. The SR830 Lock-In Amplifier . . . . .	19
3.2. Pre-amplifier . . . . .	21
3.3. Noise sources . . . . .	22
3.3.1. Johnson-Nyquist noise . . . . .	22
3.3.2. Flicker noise . . . . .	23
3.3.3. Ground loops . . . . .	23
3.3.4. Shielded conductors . . . . .	23
3.3.5. The laboratory ground . . . . .	25
3.3.6. Proper grounding . . . . .	25
3.4. Experimental setup . . . . .	26
3.4.1. Beam path . . . . .	28
3.5. Laser intensity . . . . .	29
3.6. TMR measurement . . . . .	29

3.7. Wire bonder . . . . .	30
<b>4. Experimental results</b>	<b>33</b>
4.1. General approach . . . . .	33
4.2. Laser power . . . . .	34
4.3. Beam waist measurements . . . . .	35
4.4. Dependence on the insulator thickness . . . . .	37
4.4.1. The investigated samples . . . . .	37
4.4.2. TMR measurement . . . . .	37
4.4.3. TMS effect in detail . . . . .	39
4.4.4. Power dependence of the TMS effect . . . . .	40
4.4.5. Time resolved Seebeck signal . . . . .	42
4.4.6. Position dependence of the TMS effect . . . . .	45
4.4.7. Position dependence - time resolved . . . . .	46
4.5. Sample with exchange bias . . . . .	49
4.5.1. TMR measurement . . . . .	49
4.5.2. TMS measurement in detail . . . . .	50
4.5.3. TMS - position dependent measurement . . . . .	51
4.5.4. TMS - power dependent measurement . . . . .	52
4.5.5. Time dependent Seebeck voltage. . . . .	52
4.5.6. MTJs as capacitors . . . . .	53
4.5.7. Thermal diffusion in silicon . . . . .	54
4.6. Thermal simulation . . . . .	56
<b>5. Summary</b>	<b>61</b>
5.1. Influence of the MgO barrier . . . . .	61
5.2. Outlook . . . . .	62
<b>A. Laser intensity</b>	<b>63</b>
A.1. Determining the beam waist . . . . .	63
A.2. Calculating the intensity . . . . .	66
<b>Bibliography</b>	<b>67</b>
<b>Acknowledgment</b>	<b>69</b>

# 1. Introduction

In this Bachelor thesis the magneto-Seebeck effect (TMS effect) in magnetic tunnel junctions is investigated. A magnetic tunnel junction (MTJ) is built with two ferromagnetic layers, here CoFeB, separated by an insulating MgO layer. A laser is used to heat the MTJ, thus creating a temperature gradient in the MTJ. This temperature gradient causes a Seebeck voltage which depends on the relative magnetic alignment of the two CoFeB layers. The reason is that the charge-based Seebeck coefficients depend on the magnetic configuration of the sample.

The magneto-Seebeck effect combines the research fields of thermo-electric effects with magneto-electric effects. In general, the investigated MTJs are of great scientific interest, because the TMR effect can also be observed in these systems and so they can be used for new computer storage devices like MRAM. For this reason, the thermoelectric properties of such systems are also interesting. Possible applications for the magneto-Seebeck effect could be the readout of storage devices using just waste heat produced by other integrated circuits.

The aim of this work is to investigate the magneto-Seebeck effect for different compositions of the layers in the MTJ. Particularly the influence of the thickness of the insulating MgO barrier on the magneto-Seebeck effect will be determined. Additionally, a system with exchange bias will be investigated. This exchange bias is caused by an antiferromagnetic layer and prevents one ferromagnetic layer from changing its magnetic alignment.

At the beginning of this thesis, the theoretical aspects concerning the TMR effect and the magneto-Seebeck effect will be explained. Afterwards, the experimental setup will be presented in detail. The measurement devices used in this experiment will be focused on, in particular, and explanations to the noise sources that have to be considered when measuring small voltages in the order of nano volts will be given. In the experimental part of this thesis, first measurements with a series of samples which differ only in the MgO barrier high will be discussed to determine

the influence of the MgO barrier. A sign change in the magneto-Seebeck effect as a function of the applied laser intensity can be observed which shifts to higher laser intensities for thinner barriers. After that the TMS measurements on a sample with exchange bias are discussed. Furthermore, the influence of the substrate will be pointed out in this section. The MTJs are considered as capacitors and the influence of thermal diffusion in the substrate is determined. The last part of this chapter is concerned with thermal simulations to calculate the temperature gradient in the MTJ. Thus, it will be possible to calculate the Seebeck coefficients for parallel and antiparallel alignment and different temperatures.

As a general result it appears that the MgO barrier has a strong influence on the magneto-Seebeck signal. But also the substrate on which the MTJs are grown has an influence on the measurements. This is confirmed by the time dependent voltage signal.

## 2. Theoretical background

### 2.1. Tunnel Effect in the Simmons model

The quantum-mechanical tunnel effect is the basis for many physical processes. It is especially important for the understanding of the TMR effect. If a voltage is applied to two electrodes which are separated by a very thin insulator, a current will be observed. This effect cannot be described with classical physics, but only with quantum mechanics. In 1963, the tunnel effect was theoretically investigated for a potential barrier with an arbitrary shape by *Simmons* [11].

From the WKB approximation, the probability  $D(E)$  that an electron with the energy  $E$  can penetrate a potential barrier  $\Phi(x)$ , is known [15, page 250]:

$$D(E) = \exp\left(-\frac{4\pi}{\hbar} \int_{s_1}^{s_2} \sqrt{2m(\Phi(x) - E)} dx\right). \quad (2.1)$$

Here  $\Delta s = s_2 - s_1$  is the width of the potential wall and  $\Phi(x)$  its shape. Now, the current density  $J$  is given by [11]:

$$J = \left(\int_0^{E_m} D(E) dE\right) \cdot \left(\frac{4\pi m^2 e}{\hbar^3} \int_0^\infty f(E) - f(E + eV) dE\right). \quad (2.2)$$

$E_m$  is the maximum energy of the electrons in the electrodes,  $f(E)$  the Fermi-Dirac distribution and  $V$  the applied voltage. The first integral expression gives the possibility that electrons with an energy between 0 and  $E_m$  tunnel through the insulator. The second integral describes the number of electrons in the first electrode which can access free states in the second electrode. It is an essential condition to have free states in the second electrode that can be occupied by the tunneling electrons. In figure 2.1, the Fermi functions at  $T = 0$  K for the two electrodes are depicted. The area marked in bright red corresponds with the integral expression.

## 2. Theoretical background

If there is no voltage applied between the electrodes, the tunnel current will be zero. In the picture in figure 2.1 both Fermi functions would overlap exactly. So the area which describes the number of tunneling electrons would be zero, also. In fact, electrons would tunnel also if the applied voltage is zero. But the current in both directions would be equal so there is no net current.

To perform the integration for an arbitrary potential  $\Phi(x) = E_F + \varphi(x)$ , the potential is approximated by the mean barrier height:

$$\bar{\varphi} = \frac{1}{\Delta s} \int_{s_1}^{s_2} \varphi(x) dx \quad (2.3)$$

and the temperature is set to  $T = 0$  K, so the Fermi-Dirac distribution is a step function. In this case equation (2.2) can be approximated with the following term [11]:

$$J \approx \frac{e}{2\pi\hbar(\beta\Delta s)^2} \left( \bar{\varphi} \exp\{-A\sqrt{\bar{\varphi}}\} - (\bar{\varphi} + eV) \exp\{-A\sqrt{(\bar{\varphi} + eV)}\} \right), \quad (2.4)$$

where

$$A = \frac{4\pi\beta\Delta s\sqrt{2m}}{\hbar}. \quad (2.5)$$

$\beta$  is a correction factor that will be explained later. Equation (2.4) can be interpreted as a current density  $J_1 = J_0 \bar{\varphi} \exp\{-A\sqrt{\bar{\varphi}}\}$  flowing in one direction and a second current density  $J_2 = J_0 (\bar{\varphi} + eV) \exp\{-A\sqrt{(\bar{\varphi} + eV)}\}$  flowing in the other direction. For plausibility check, one can consider the case that no voltage is applied ( $V = 0$ ) to the electrodes.  $J_1$  will then equal  $J_2$  and there is no net current. In the special case of an intermediate voltage range ( $V < \varphi_{\max}/e$ ), which is typical for tunnel experiments,  $\beta$  can be set to one in good approximation. The error in the exponent of equation (2.4) will be 6% if  $V = \varphi_{\max}/e$ . But the error decreases rapidly if  $V$  is reduced. For  $V = 0.75\varphi_{\max}/e$  the error amounts to just 1%.

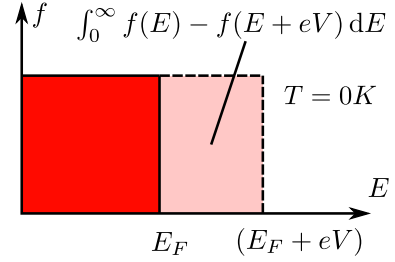


**Figure 2.1.:** Fermi functions for two electrodes with applied voltage  $V$ .

## 2.2. Tunneling magneto resistance

In the previous section, the tunnel current between two metal electrodes was described. In the case of magnetic electrodes separated by an insulator the TMR effect can occur. This means that the tunnel current depends on the relative magnetization between the two electrodes. The definition of the TMR effect is [9]

$$\text{TMR} = \frac{R_{\text{AP}} - R_{\text{P}}}{R_{\text{P}}}, \quad (2.6)$$

with  $R_{\text{P}}$  and  $R_{\text{AP}}$  being the resistance in parallel and antiparallel magnetic alignment, respectively.

### 2.2.1. The Julliere model

The TMR effect was first observed by Julliere in Fe/Ge/Co tunnel junctions at very low temperatures  $T \leq 4.2$  K [8]. For ferromagnetic layers, the spin degree of freedom has to be considered during the tunnel process. Consequently, Julliere introduced a two current model for electrons with spin-up and spin-down. The total current is the sum for spin-up and spin-down current:

$$I = I_{\uparrow} + I_{\downarrow}. \quad (2.7)$$

In the Julliere model the inelastic electron tunneling is neglected. So there are no spin flips assumed and the spin is conserved during the tunnel process. The ansatz for the Julliere model is that the tunnel currents for parallel and antiparallel magnetization are proportional to the product of the density of states in both electrodes left (L) and right (R) [1, page B2.5]

$$I_{\text{P}} \propto \mathcal{D}_{\text{L}\uparrow} \cdot \mathcal{D}_{\text{R}\uparrow} + \mathcal{D}_{\text{L}\downarrow} \cdot \mathcal{D}_{\text{R}\downarrow}, \quad (2.8)$$

$$I_{\text{AP}} \propto \mathcal{D}_{\text{L}\uparrow} \cdot \mathcal{D}_{\text{R}\downarrow} + \mathcal{D}_{\text{L}\downarrow} \cdot \mathcal{D}_{\text{R}\uparrow}. \quad (2.9)$$

For a fixed bias voltage, the current is inversely proportional to the resistance of the tunnel junction ( $I \propto 1/R$ ). So, concerning equation (2.6), the TMR ratio can

be written as

$$\text{TMR} = \frac{R_{\text{AP}} - R_{\text{P}}}{R_{\text{P}}} = \frac{I_{\text{P}} - I_{\text{AP}}}{I_{\text{AP}}} = \frac{(\mathcal{D}_{\text{L}\uparrow} - \mathcal{D}_{\text{L}\downarrow})(\mathcal{D}_{\text{R}\uparrow} - \mathcal{D}_{\text{R}\downarrow})}{\mathcal{D}_{\text{L}\uparrow} \cdot \mathcal{D}_{\text{R}\uparrow} + \mathcal{D}_{\text{L}\downarrow} \cdot \mathcal{D}_{\text{R}\downarrow}}. \quad (2.10)$$

The definition of the spin polarization from *Tedrow* [14],

$$P = \frac{\mathcal{D}_{\uparrow} - \mathcal{D}_{\downarrow}}{\mathcal{D}_{\uparrow} + \mathcal{D}_{\downarrow}}, \quad (2.11)$$

implies for the TMR ratio

$$\text{TMR} = \frac{2P_{\text{L}}P_{\text{R}}}{1 - P_{\text{L}}P_{\text{R}}}. \quad (2.12)$$

Here  $P_{\text{L}}$  is the spin polarization of the left electrode and  $P_{\text{R}}$  of the right electrode. The Julliere model explains very well the basic features of the TMR effect: If the spin polarization of one electrode is 0%, no TMR effect will be observed. For 100% spin polarization of both electrodes the TMR effect is maximal and the TMR ratio becomes infinite. As a consequence  $R_{\text{AP}}$  becomes infinity too, so there is no tunnel current if the electrodes are aligned antiparallel. The definition of the spin polarization (equation (2.11)) implies, that  $P$  is always positive, leading to a positive TMR ratio. Thus, the resistance in antiparallel alignment is always bigger than the resistance in parallel alignment.

On the other hand, a big weakness of the Julliere model is that the density of states  $\mathcal{D}$  is not very well defined. It is related to the density of states near the Fermi level  $E_{\text{F}}$ , but there is no exact definition. Therefore, the application of the Julliere model is limited.

### 2.2.2. Model by Butler et al.

Butler et al. used first principle electronic structure techniques to calculate the tunneling in Fe(100)/MgO(100)/Fe(100) sandwiches [2]. To compute the tunnel conductance, they used the Landauer conductance formula

$$G = \frac{e^2}{h} \sum_{k_{\parallel}, j} T^{+}(k_{\parallel}, j). \quad (2.13)$$

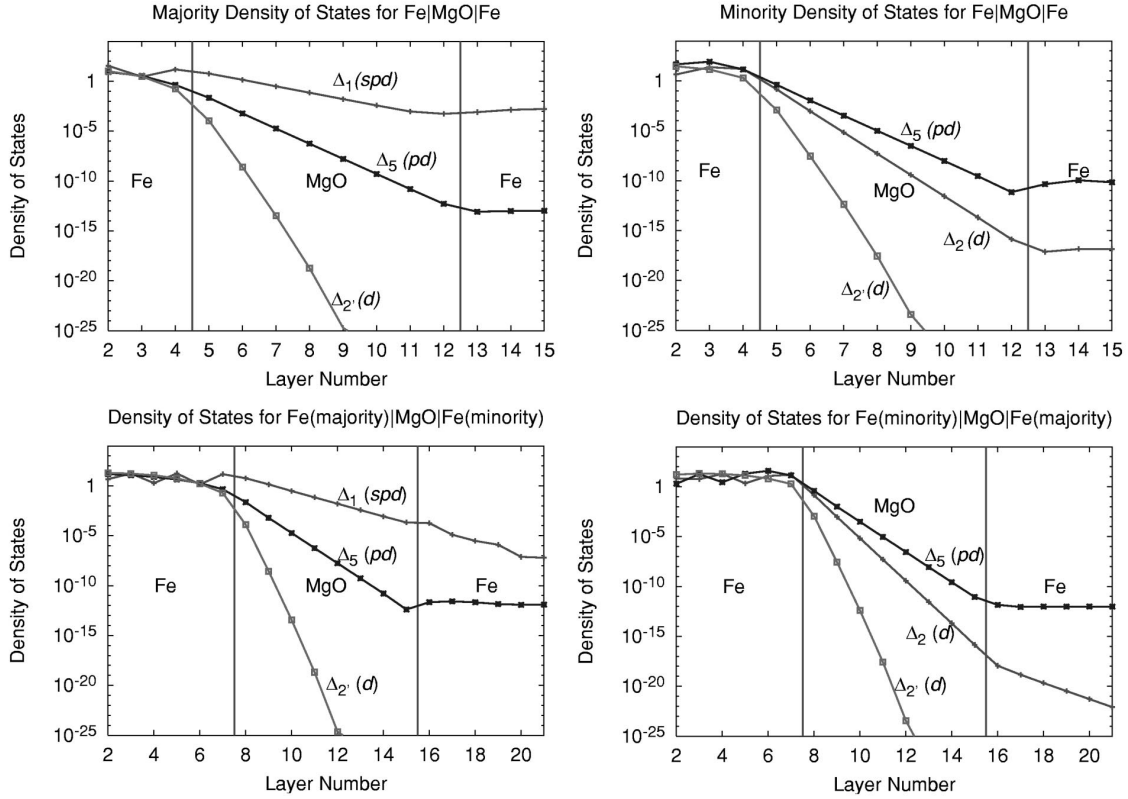


**Figure 2.2.:** Tunneling DOS in Fe|MgO|Fe sandwich for parallel and antiparallel magnetic alignment in majority and minority channel [2].

The conduction depends on the probability of a Bloch electron being transmitted from one Fe layer through the MgO barrier into the second Fe layer. The sum over  $j$  must be taken into account because there may be more than one Bloch state for a given  $k_{||}$ . A Fe/MgO/Fe tunnel junction is a good object for these investigations because MgO grows epitaxial on Fe. In fact, Fe has nearly the same lattice constant as MgO.

Figure 2.2 shows the tunneling density of states (DOS) for a Fe/MgO/Fe system with 8 MgO layers and  $k_{||} = 0$ . The tunneling DOS means that there are incoming Bloch states with unit flux on the left hand side and corresponding transmitted Bloch states on the right side. Here the case for  $k_{||} = 0$  is considered because the transmission in the majority channel is than maximized.

As well as the majority channel, the minority channel has four Fe(100) Bloch states.

The  $\Delta_5$  state is doubly degenerate. In contrast to the majority channel, the minority channel has no  $\Delta_1$  state but a  $\Delta_2$  state. The  $\Delta_1$  state decays as evanescent state in the MgO and has the slowest decay rate. So the conductance is highest for the  $\Delta_1$  band and thus also highest for the majority channel. The second slowest decaying band is the  $\Delta_5$  band for both majority and minority channel. So the conductance of the minority channel is determined by this state.

For antiparallel magnetic alignment there is also a  $\Delta_1$  state (figure 2.2 bottom left). This state decays again in the MgO but it can not propagate in the second Fe layer, because there is no  $\Delta_1$  state near the Fermi energy. Thus, it continues to decay and the  $\Delta_1$  state is totally reflected. The state  $\Delta_5$  on the other hand decays faster, but is able to enter the second layer. So this band is responsible for conduction in the antiparallel state.

In general it is important to have free Bloch states after the tunnel barrier for the tunneling electrons.

Additionally Butler et al. calculated the conductance for majority and minority channel as well as the conductance for parallel alignment. The results are plotted in figure 2.3. In case of thin layers smaller than 8 mono layers, the conductance in the minority channel is bigger than the conductance for antiparallel alignment. The conductance in the majority state is always largest (because of the  $\Delta_1$ -symmetry state). The difference between conductance in majority state (parallel alignment) and antiparallel alignment becomes bigger for more MgO layers. As a consequence, the TMR ratio increases with the number of MgO layers.

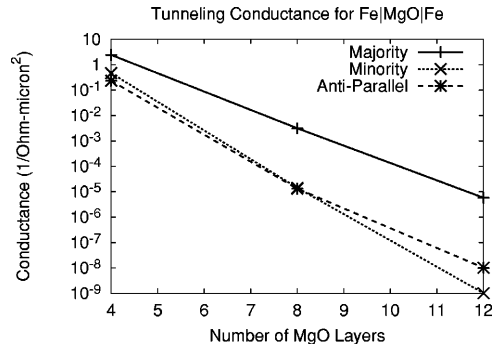


**Figure 2.3.:** Tunneling conductance for different thicknesses of MgO layers [2].

## 2.3. Classical Seebeck Effect

**Dynamic equations** The Seebeck effect was discovered in 1821 by Thomas Johann Seebeck. It is a thermo-electric effect because it describes the conversion of tem-

perature directly into electric current. For a derivation, the dynamic equations are needed [3, page 296]:

$$-J_N = L_{11} \frac{1}{T} \nabla \mu + L_{12} \nabla \frac{1}{T}, \quad (2.14)$$

$$J_Q = L_{12} \frac{1}{T} \nabla \mu + L_{22} \nabla \frac{1}{T}. \quad (2.15)$$

Here  $J_N$  describes the current density of electrons per unit volume and  $J_Q$  the current density of heat.  $T$  is the temperature and  $\mu$  the chemical potential. The  $L_{jk}$  are kinetic coefficients. These coefficients are functions of intensive parameters and can be expressed as a derivative of the flux with respect to the corresponding intensive parameter

$$L_{jk} = \left( \frac{\partial J_k}{\partial \mathfrak{F}_j} \right)_0, \quad (2.16)$$

where  $\mathfrak{F}_j$  is the intensive parameter. For simplification of the dynamic equations, the Onsager theorem in the absence of a magnetic field was used, which states that  $L_{12} = L_{21}$ .

**Seebeck effect** The experimental set-up to observe the Seebeck effect is sketched in figure 2.4. Two different metals A and B (indicated by white and black dots) are contacted at two different junctions. Additionally, there is a temperature gradient so that the temperature at junction 1 is higher than at junction 2. In metal B a voltmeter is inserted. It is assumed that this voltmeter behaves like an ideal voltmeter, meaning that its resistance is infinity (no current in the circuit), but it allows the flow of heat. The temperature at the location of the voltmeter is  $T'$ . Because no electric current is allowed to pass the voltmeter, the current density of electrons  $J_N$  is equal to zero. From

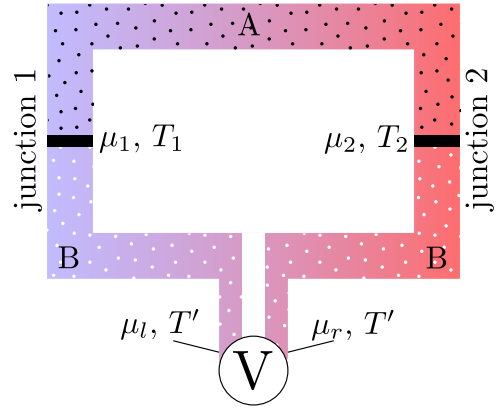


**Figure 2.4.:** Thermocouple with two metals A and B at different temperatures 1 and 2.

## 2. Theoretical background

---

the first dynamic equation (2.14) then follows

$$\nabla\mu = \frac{L_{12}}{TL_{11}}\nabla T. \quad (2.17)$$

This equation can be integrated along the different metal wires:

$$\mu_2 - \mu_1 = \int_{T_1}^{T_2} \frac{L_{12}^A}{TL_{11}^A} dT, \quad (2.18)$$

$$\mu_2 - \mu_r = \int_{T_r}^{T_2} \frac{L_{12}^B}{TL_{11}^B} dT, \quad (2.19)$$

$$\mu_l - \mu_1 = \int_{T_1}^{T_l} \frac{L_{12}^B}{TL_{11}^B} dT. \quad (2.20)$$

These three equations are summarized in one equation. By substituting equation (2.19) and (2.20) into equation (2.18) one gets:

$$\mu_r - \mu_l = \int_{T_1}^{T_2} \frac{L_{12}^A}{TL_{11}^A} dT - \int_{T_r}^{T_2} \frac{L_{12}^B}{TL_{11}^B} dT - \int_{T_1}^{T_l} \frac{L_{12}^B}{TL_{11}^B} dT = \int_{T_1}^{T_2} \frac{L_{12}^A}{TL_{11}^A} - \frac{L_{12}^B}{TL_{11}^B} dT.$$

It is assumed that there is no temperature gradient across the voltmeter. The voltage generated by the temperature gradient can then be written as

$$V = \frac{1}{e}(\mu_r - \mu_l) = \int_{T_1}^{T_2} \underbrace{\frac{L_{12}^A}{eTL_{11}^A}}_{S_A(T)} - \underbrace{\frac{L_{12}^B}{eTL_{11}^B}}_{S_B(T)} dT. \quad (2.21)$$

In this equation, the Seebeck coefficients for both metals  $S_A(T)$  and  $S_B(T)$  can be defined. These coefficients depend nonlinearly on the temperature but also on the material and the material structure. If the Seebeck coefficients are constant in the temperature range of interest, the integral expression (2.21) can be simplified

$$V = (S_A - S_B)(T_2 - T_1) \Rightarrow \Delta S = (S_B - S_A) = -\frac{V}{\Delta T}. \quad (2.22)$$

Thus, a possibility to measure the Seebeck coefficient of a metal is to measure the voltage of a thermo couple for a known temperature gradient.

## 2.4. Magneto-Seebeck effect

The Magneto-Seebeck effect is a thermo-electrical effect. A temperature gradient applied along a sandwich ferromagnet/insulator/ferromagnet causes a Seebeck voltage which depends on the relative magnetic alignment of the two ferromagnetic layers. Thus, the magneto-Seebeck effect is similar to the TMR effect. But in principle these are two different effects. This means, a high TMR effect does not require a high TMS effect.

The magneto-Seebeck effect can be explained with a change of the Seebeck coefficients during a transition from parallel to antiparallel magnetization. The definition of the magneto-Seebeck effect is [4]

$$S_{\text{MS}} = \frac{S_{\text{P}} - S_{\text{AP}}}{\min(|S_{\text{P}}|, |S_{\text{AP}}|)}. \quad (2.23)$$

Here  $S_{\text{P}}$  is the Seebeck coefficient for parallel magnetization and  $S_{\text{AP}}$  for antiparallel magnetization. Heiliger et al. used ab initio calculations to determine the Seebeck coefficients. First, the transmission function through the tunnel barrier  $T(E)$  is calculated with the non-equilibrium Green's function method implemented in the Korringa-Kohn-Rostoker algorithm. Afterwards the moments  $L_n$  can be calculated [4]

$$L_n = \frac{2}{\hbar} \int T(E)(E - \mu)^n (-\partial_E f(E, \mu, T)) \, dE, \quad (2.24)$$

where only the derivative of the Fermi function  $f$  is temperature dependent but not the transmission function  $T$ . With the moments it is possible to calculate the Seebeck coefficients and thus the Seebeck effect. The Seebeck coefficients are given by [4]

$$S = -\frac{1}{eT} \frac{L_1}{L_0} = -\frac{1}{eT} \frac{\int T(E)(E - \mu)(-\partial_E f(E, \mu, T)) \, dE}{\int T(E)(-\partial_E f(E, \mu, T)) \, dE}. \quad (2.25)$$

If the moments are evaluated, it is also possible to calculate the conductance  $G$ :

$$G = e^2 L_0 = \frac{2e^2}{\hbar} \int T(E)(E - \mu)(-\partial_E f(E, \mu, T)) \, dE. \quad (2.26)$$

## 2. Theoretical background

It is useful to visualize these quantities geometrically. In figure 2.5 a hypothetical transmission function  $T(E)$  is drawn, for parallel magnetization (left) and for antiparallel magnetization (right). The conductance  $G$  (equation (2.26)) is an integral over the transmission function, weighted with the derivative of the Fermi function. Thus it can be presented as an area. In figure 2.5 this area is marked in dark red and dark blue for parallel and antiparallel magnetization respectively. Because the area for parallel magnetization is much bigger than for antiparallel magnetization, a high TMR ratio can be expected in both cases.

On the other hand, equation (2.25) is the geometric center of mass of the function  $T(E)\partial_E f(E, \mu, T)$ . Thus, it can be represented as a single value (line in figure 2.5). In the upper case both values for  $S_P$  and  $S_{AP}$  differ. So a high magneto Seebeck effect occurs. In the other case both values are equal. Thus the  $S_{SM}$ -ratio is zero even if there is a high TMR ratio. In general, the magneto-Seebeck effect depends on the exact composition of the ferromagnetic layer, on the barrier thickness and on the base temperature. Heiliger et al. calculated the Seebeck coefficients for CoFe/MgO/CoFe sandwiches. CoFe is assumed to have alternating layers of Co and Fe which are parallel to the Fe-MgO interface. Thus three different cases for the two interfaces between MgO and CoFe can be distinguished:

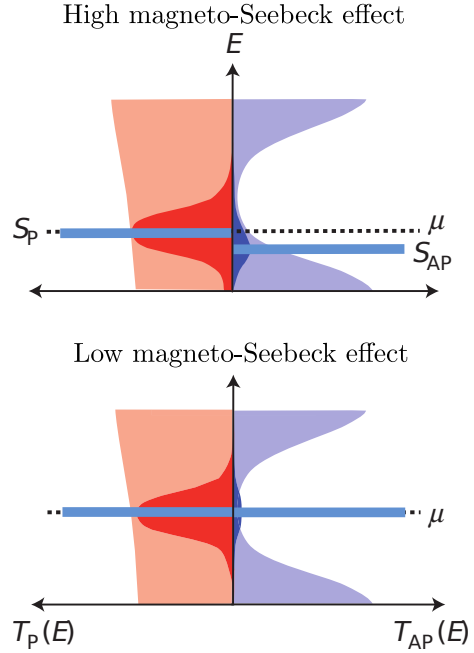


**Figure 2.5.:** Transmission function  $T(E)$  and Seebeck coefficients [16].

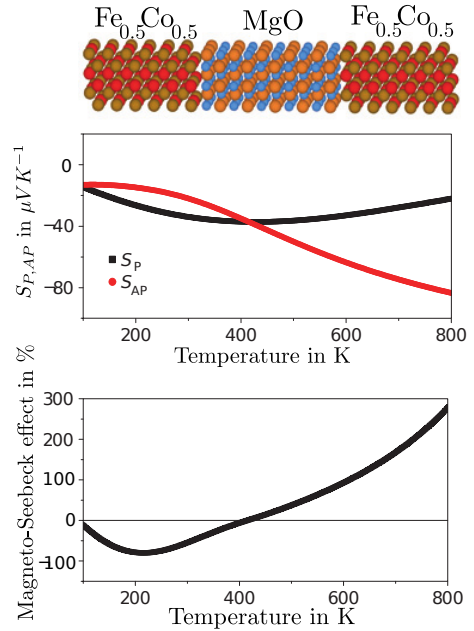


**Figure 2.6.:** Temperature dependence of the magneto-Seebeck effect in a bcc lattice [16].

- on both sides Fe is the next layer to MgO  $\rightarrow$  CoFe/MgO/FeCo
- on both sides Co is the next layer to MgO  $\rightarrow$  FeCo/MgO/CoFe
- on one side Fe is the next layer to MgO, on the other side Co  $\rightarrow$  CoFe/MgO/CoFe

In figure 2.7 the Seebeck effect and the Seebeck coefficients in parallel and antiparallel alignment are plotted for these three cases. Additionally, barrier thicknesses of 6 mono layers and 10 mono layers are plotted.

In general, there is a strong influence of the interface termination on the magneto-Seebeck effect. A trend is that  $S_{MS}$  is positive for all interface terminations. In the case of different interface terminations  $S_{MS}$  has the highest value. A similarity is that all curves for  $S_{MS}$  have a minimum roughly at room temperature. The values for high temperatures may have a big error because the transmission function is assumed to have no temperature dependence which could be a crucial simplification for high temperatures. In case of the Fe termination on both sides there is a divergence for thinner barriers at 150 K because the Seebeck coefficient for the parallel alignment becomes zero. One interesting point is that the divergence in the

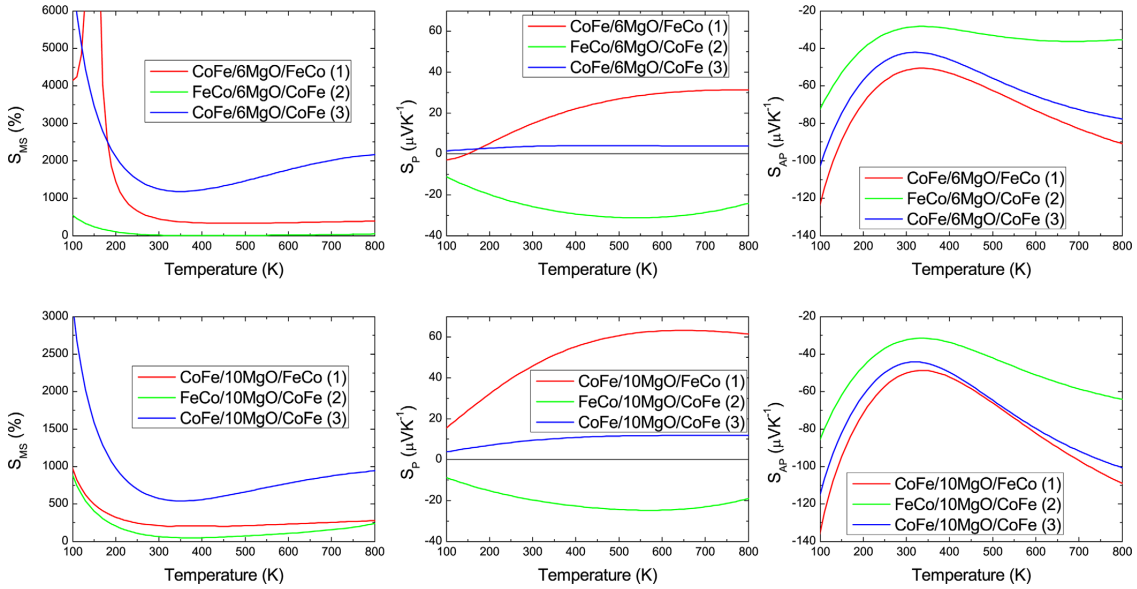


**Figure 2.7.:** Temperature dependence of the magneto-Seebeck effect and the Seebeck coefficients for different layer compositions [4].

## 2. Theoretical background

magneto-Seebeck effect vanishes in ten mono layer MgO barriers. For both MgO layer thicknesses the Seebeck coefficients in antiparallel cases are negative and have a maximum at room temperature.

Additionally, the Seebeck coefficients and the magneto-Seebeck effect for  $\text{Co}_{0.5}\text{Fe}_{0.5}$  in a bcc lattice and a 10 mono layer thick MgO barrier have been calculated (figure 2.6). The behavior in this configuration changes. For example the Seebeck coefficients are always negative. The magneto-Seebeck effect is also predicted to be negative for temperatures smaller than 400 K and thus also at room temperature.

In experiments it is unlikely to have alternating layers of Co and Fe, so the bcc structure is more realistic. However, if sputtered thin films are investigated in an experiment, one would expect a disordered alloy. A simple idea to realize disordered alloys in a simulation is proposed by Heiliger et al. [4]. A disordered junction can be seen as a parallel circuit of ordered micro junctions. If the atoms in the alloy are ordered randomly, the probability to have FeCo/MgO/CoFe or CoFe/MgO/FeCo micro junctions is each 25% and the probability for a FeCo/MgO/FeCo junction is 50%. Because a parallel circuit of micro junctions is considered, the transmission functions can just be added up. For the magneto-Seebeck effect follows [4]

$$S_{\text{MS}} = \frac{0.25S_1G_1 + 0.25S_2G_2 + 0.5S_3G_3}{0.25G_1 + 0.25G_2 + 0.25G_3}.$$

Figure 2.8 shows the magneto-Seebeck effect calculated with this equation. For only 6 MgO layers, there is still a divergence for the  $S_{\text{MS}}$  effect. But this divergence vanishes again for 10 MgO layers. In this model, the magneto-Seebeck effect is never negative.

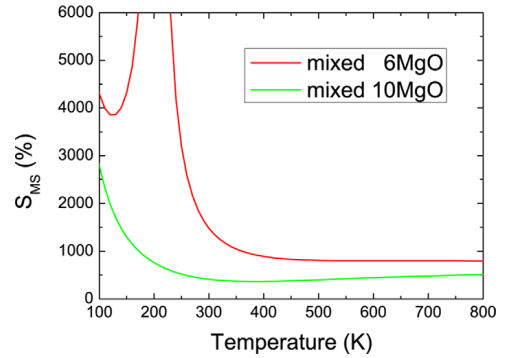


**Figure 2.8.:** Magneto-Seebeck effect for an disordered FeCo alloy [4].

## 3. Experimental setup

### 3.1. Lock-In Amplifier

When measuring the Seebeck effect it is essential to detect very small voltages in the order of nano volts. Therefore, we use first a pre-amplifier followed by a lock-in amplifier. It is important to understand how the amplification works.

#### 3.1.1. General Principle

With a lock-in amplifier it is possible to detect AC signals with a certain frequency. This principle is called *phase sensitive detection*. The frequency for the measurement can be set by a function generator. This signal is called the reference signal. Internally, the lock-in amplifier has a function generator which can be phase locked to the reference frequency (phase locked loop PLL). The output of the function generator is a sine wave with the same frequency as the reference signal and a constant additional phase

$$U_{\text{PLL}}^1 = U_{\text{PLL}}^0 \sin(\omega_{\text{ref}} \cdot t + \vartheta_{\text{PLL}}) . \quad (3.1)$$

The signal, which is measured with the lock-in amplifier is assumed to have a frequency  $\omega_{\text{sig}}$  and an amplitude  $U_{\text{sig}}^0$

$$U_{\text{sig}} = U_{\text{sig}}^0 \sin(\omega_{\text{sig}} \cdot t + \vartheta_{\text{sig}}) . \quad (3.2)$$

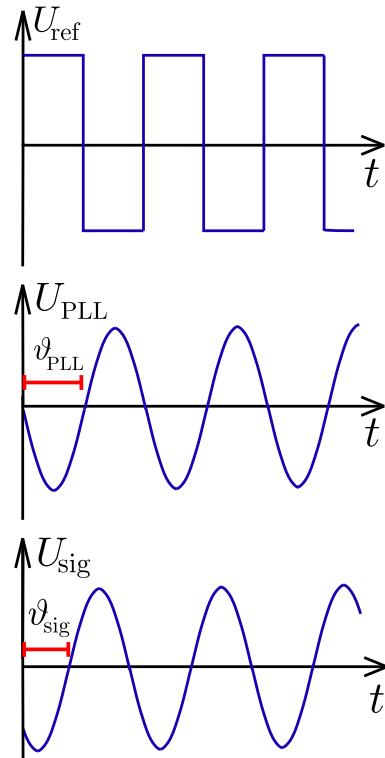


**Figure 3.1.:** Signal processing of the lock-in amplifier.

### 3. Experimental setup

---

Now the lock-in amplifier has a so-called phase sensitive detector (PSD) which multiplies both voltage signals. With the use of an addition theorem one gets:

$$U_{\text{PSD}}^1 = U_{\text{PLL}}^1 \cdot U_{\text{sig}} = U_{\text{PLL}}^0 U_{\text{sig}}^0 \sin(\omega_{\text{ref}} \cdot t + \vartheta_{\text{PLL}}) \sin(\omega_{\text{sig}} \cdot t + \vartheta_{\text{sig}}) \quad (3.3)$$

$$= 0.5 \cdot U_{\text{PLL}}^0 U_{\text{sig}}^0 (\cos([\omega_{\text{ref}} - \omega_{\text{sig}}]t + \vartheta_{\text{PLL}} - \vartheta_{\text{sig}})) \quad (3.4)$$

$$- \cos([\omega_{\text{ref}} + \omega_{\text{sig}}]t + \vartheta_{\text{PLL}} + \vartheta_{\text{sig}})). \quad (3.5)$$

So it is possible to write the multiplied signals as a sum of two cosine functions, one with a frequency  $\omega_{\text{ref}} + \omega_{\text{sig}}$  and one with the frequency  $\omega_{\text{ref}} - \omega_{\text{sig}}$ . The last element of a lock-in amplifier is a low pass filter which attenuates signals with a frequency higher than  $\omega_{\text{pass}}$ . If  $\omega_{\text{pass}}$  is chosen small enough, there is no output in the general case. But if both frequencies  $\omega_{\text{ref}}$  and  $\omega_{\text{sig}}$  are equal, the argument of the first cosine is time independent. Thus with a perfect low pass filter, which suppresses all frequencies bigger than zero, one would get a constant signal that is proportional to the input voltage:

$$U_{\text{lock-in}}^1 = 0.5 \cdot U_{\text{PLL}}^0 U_{\text{sig}}^0 \cos(\vartheta_{\text{PLL}} - \vartheta_{\text{sig}}). \quad (3.6)$$

In case of a low-pass filter, which is not ideal, signals with frequencies near the reference frequency will also result in an output signal. But the general result is that the lock-in amplifier detects only signals with a special frequency equal to the reference frequency.

However, the output signal still depends on the relative phase  $\vartheta_{\text{sig}} - \vartheta_{\text{ref}}$ . This problem can be managed with the use of a second phase sensitive detector. This phase sensitive detector does not multiply the signal with the same sine function as the first PSD but with a phase shifted sine function. The phase shift is  $\pi/2$  and the voltage at the second PSD is as follows:

$$U_{\text{PLL}}^2 = U_{\text{PLL}}^0 \sin\left(\omega_{\text{ref}} \cdot t + \vartheta_{\text{PLL}} - \frac{\pi}{2}\right). \quad (3.7)$$

The signal after the low-pass filter can be calculated in the same way as above:

$$U_{\text{lock-in}}^2 = 0.5 \cdot U_{\text{PLL}}^0 U_{\text{sig}}^0 \cos\left(\vartheta_{\text{PLL}} - \frac{\pi}{2} - \vartheta_{\text{sig}}\right) \quad (3.8)$$

$$= 0.5 \cdot U_{\text{PLL}}^0 U_{\text{sig}}^0 \sin(\vartheta_{\text{PLL}} - \vartheta_{\text{sig}}). \quad (3.9)$$

In the next step new variables  $X$ ,  $Y$  and  $\vartheta = \vartheta_{\text{PLL}} - \vartheta_{\text{sig}}$  are introduced:

$$X = \frac{U_{\text{lock-in}}^1}{0.5 \cdot U_{\text{PLL}}^0} = U_{\text{sig}}^0 \cdot \cos(\vartheta) , \quad (3.10)$$

$$Y = \frac{U_{\text{lock-in}}^2}{0.5 \cdot U_{\text{PLL}}^0} = U_{\text{sig}}^0 \cdot \sin(\vartheta) . \quad (3.11)$$

These variables are calculated and outputted by the lock-in amplifier.  $X$  can be interpreted as the real part of the signal and  $Y$  as the imaginary part. Understanding the measured signal as a complex number, the absolute value  $R$  can be calculated as

$$R = \sqrt{X^2 + Y^2} = U_{\text{sig}}^0 . \quad (3.12)$$

One advantage is that this value does not depend on the phase  $\vartheta$  but only on  $U_{\text{sig}}^0$ . The relative phase between the reference signal and the detected signal can be calculated in the following way:

$$\vartheta = \arctan\left(\frac{Y}{X}\right) . \quad (3.13)$$

### 3.1.2. Measured Signal

In general, the input signal of the lock-in amplifier can be represented as Fourier series, that is a sum over many sine and cosine functions:

$$U_{\text{in}} = \frac{a_0}{2} + \sum_{n=1}^{\infty} \left[ a_n \cos\left(\frac{2\pi n}{\tau} x\right) + b_n \sin\left(\frac{2\pi n}{\tau} x\right) \right] . \quad (3.14)$$

$n$	0	1	2	3
$a_n$	1	0	0	0
$b_n$	0	$\frac{2}{\pi}$	0	$\frac{2}{3\pi}$

**Table 3.1.:** First four Fourier coefficients for a rectangular function

$a_n$  and  $b_n$  are the Fourier coefficients and  $\tau$  is the length of one interval. As shown above, the lock-in amplifier picks just the one component of this Fourier series which fulfills the relation  $2\pi n/\tau = \omega_{\text{ref}}$ . All other signals are attenuated. This is really useful, because most of the noisy background of the input signal will have another frequency as the signal.

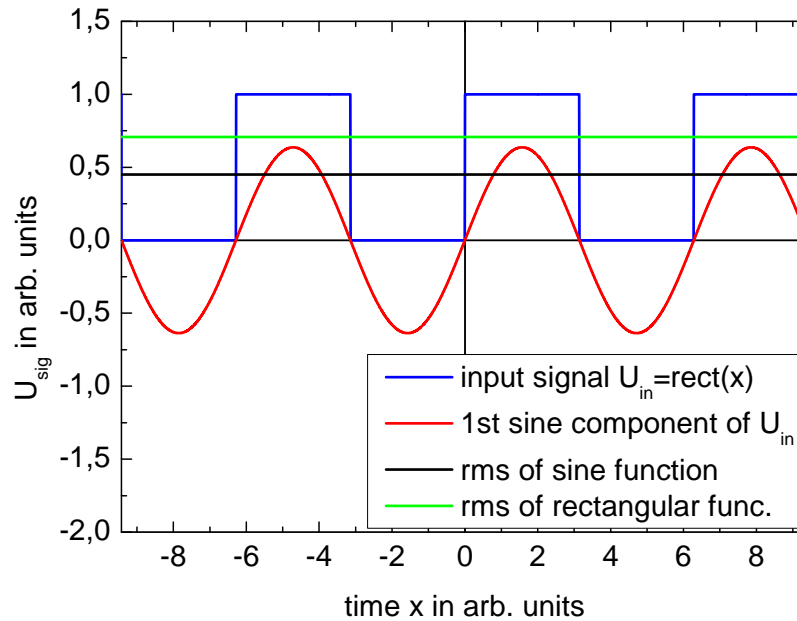


**Figure 3.2.:** Comparison between the input function of the lock-in amplifier  $U_{in} = \text{rect}(x)$  and the first sine component of this signal which is measured by the lock-in amplifier. Also the rms values of both functions are plotted.

But there is also a disadvantage of using a lock-in amplifier. In most cases the signal itself has many sine components (expecting the case that the signal is a sine function). The measured signal is not the “pure” signal anymore but only the first sine component of the signal.

This can be clarified with an example. For a rectangular signal  $U_{in}$  as shown in figure 3.2, which shall be measured with the lock-in amplifier, the Fourier components are given in table 3.1. It is assumed that the rectangular signal has the same frequency as the reference signal. Because the lock-in amplifier first removes the offset,  $a_0$  can be neglected. The lock-in detects only signals with  $\omega_{ref} = \omega_{sig}$ , so only the coefficient  $b_1$  is important. The sine functions, which belong to the other coefficients have different frequencies, so they are attenuated. In figure 3.2, the first sine component of the rectangular signal  $U_{sine}$ , which is detected, is also plotted.

Furthermore, the lock-in amplifier measures the root mean square value (rms) of

the signal and not the peak-to-peak signal. The rms value is defined by

$$U^{\text{rms}} = \sqrt{\frac{1}{T_2 - T_1} \int_{T_1}^{T_2} [U(x)]^2 dx}. \quad (3.15)$$

The integral is taken over one period. In the next step, the different rms values for the rectangular signal  $U_{\text{in}}$  and for the sine  $U_{\text{sine}}$  can be calculated:

$$U_{\text{in}}^{\text{rms}} = \sqrt{\frac{1}{2\pi} \int_0^\pi 1 dx} = \frac{1}{\sqrt{2}}, \quad (3.16)$$

$$U_{\text{sine}}^{\text{rms}} = \sqrt{\frac{1}{2\pi} \int_0^{2\pi} \left[ \frac{2}{\pi} \sin(x) \right]^2 dx} = \frac{\sqrt{2}}{\pi}. \quad (3.17)$$

Both values are plotted in figure 3.2. The important point is, that the rms value, the lock-in amplifier outputs  $U_{\text{sine}}^{\text{rms}}$ , differs from the real value  $U_{\text{in}}^{\text{rms}}$ . In addition, the output value depends on the exact time dependence of the signal. For different input signals the first sine component of a Fourier series changes and thus also the difference between input and output signal changes. This can be a problem especially for time-dependent voltage functions which do not converge fast in a Fourier series, like a sharp peak. Here the difference between input and output signal is even bigger and probably the lock-in amplifier is unsuitable for that measurement. However, in most cases the lock-in amplifier is a good choice for measuring small voltages, because with the phase sensitive detection it is possible to get a good signal to noise ratio.

### 3.1.3. The SR830 Lock-In Amplifier

The schematic block diagram of the SR830 lock-in amplifier is sketched in figure 3.3. At the lower left end one can see the reference input. The reference input can be a sine or a rectangular signal (TTL). In our experiments we used a rectangular signal as reference signal. Behind the Reference In there is an internal oscillator which provides a sine signal. This signal can be phase locked to the reference signal with the phase locked loop (PLL). The first phase shifter can change the phase of the phase locked sine generated by the internal oscillator. This phase shift will influence the  $X$  and  $Y$  value of the input voltage but not the absolute value  $R$  (see

### 3. Experimental setup

equation (3.10), (3.11) and (3.12)). After the phase shift the reference signal is multiplied with the input signal in the PSD and simultaneously again phase shifted by  $\pi/2$  and multiplied with the signal in the second PSD to measure the  $X$  and  $Y$  component. The signal outputted by the two PSDs is then low pass filtered. The settings of the low pass filter can be influenced by the time constant (t.c.). The -3 dB cut off frequency of the low pass filter is given by

$$f_{\text{cut}} = \frac{1}{2\pi \cdot \text{t.c.}} \quad (3.18)$$

The input signal is first amplified with a differential amplifier (top left in figure 3.3). The amplification can be adjusted with the dynamic reserve settings. Two notch filters behind the amplifiers remove 50 Hz and 100 Hz signals (line frequency).

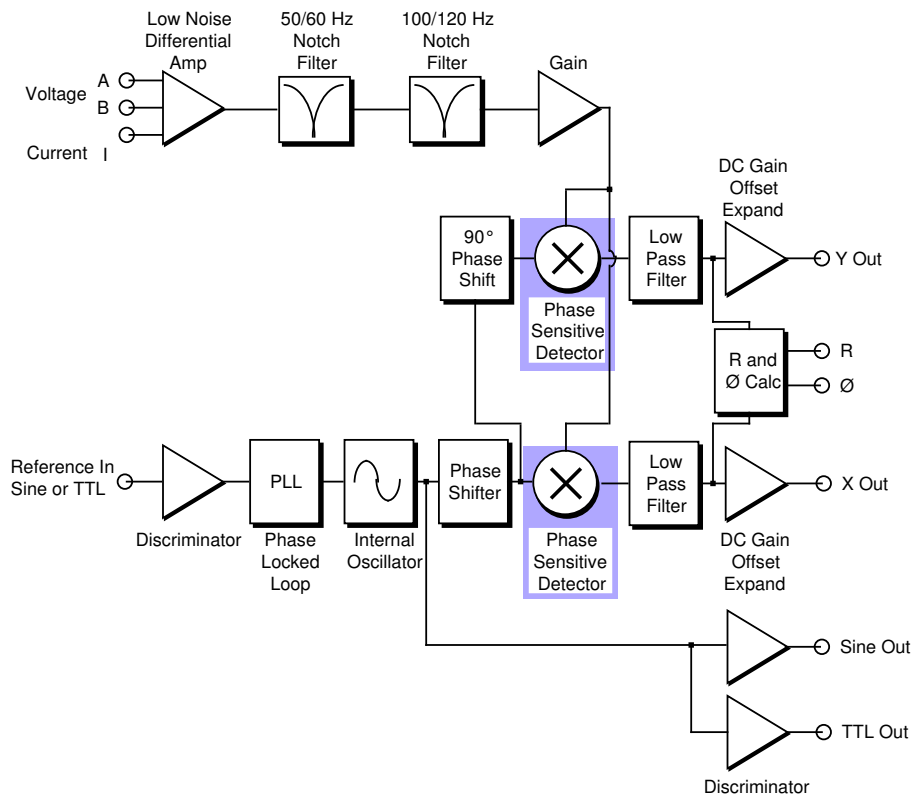


**Figure 3.3.:** Block diagram of the SR830 lock-in amplifier by Stanford Research Systems. The phase sensitive detectors are tagged in blue. [13]

## 3.2. Pre-amplifier

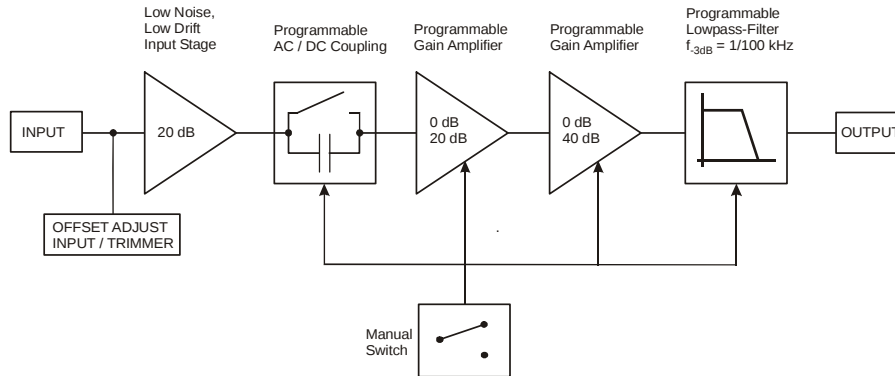


**Figure 3.4.:** Block diagram of the Femto DLPVA-100-F-S pre-amplifier. [5]

Because the occurring thermo-voltages are really small ( $\approx 100$  nV) and the input impedance of the lock-in amplifier is quite small, we use a Femto DLPVA-100-F-S pre-amplifier. This amplifier has a variable gain between 20 dB and 80 dB. However, for most measurements 60 dB gain is used. This implies the input signal is 1000 times amplified.

The amplifier is single ended. Thus the amplifier has just one reference conductor for input and output. The metal housing is also connected to the reference ground. In figure 3.4 the basic structure is shown. The offset of the input signal can be adjusted with a small screw. First the signal is amplified with 20 dB. Then one can select between AC and DC mode. AC mode would mean that the signal is expected to fluctuate around zero. Thus an offset would be removed. DC on the other hand measures the signal without adding any offset. Now, there are two more amplification stages with 20 dB and 40 dB, respectively. These gains are in series so if both gains are used, the amplification would be 60 dB plus 20 dB from the input stage. At the end of the circuit there is a low pass filter. It is adjusted in order that frequencies higher than 100 kHz are cut off. The rise/fall time of the amplifier is 3.5  $\mu$ s. So the flanks of a rectangular signal with a frequency of 1.5 kHz are steep.

If the amplifier is used in 60 dB mode, the equivalent input voltage noise will be 5.5 nV/ $\sqrt{\text{Hz}}$ . Thus, the output noise will be 5.5 mV/ $\sqrt{\text{Hz}}$ . For frequencies of 1.5 kHz only white noise is important, because the  $1/f$  corner is at 80 Hz. This means that

white noise and Flicker noise are equal for frequencies of 80 Hz. At 1.5 kHz Flicker noise is completely negligible.

As mentioned above, the Femto amplifier has a high input impedance of 1 T $\Omega$ . This is important because tunnel junctions can have a big resistance too. But it has to be assured that the voltage drops off mostly at the measurement device and not at the sample. The input impedance of the lock-in amplifier is 100 times smaller (10 M $\Omega$ ).

## 3.3. Noise sources

Because Seebeck voltages in magnetic tunnel junctions are really small, noise can be a big problem. There are different noise sources. Some have a physical origin (intrinsic noise sources), others have an external origin like the experiment design.

### 3.3.1. Johnson-Nyquist noise

Johnson-Nyquist noise is thermal noise. It is caused by the random thermal motion of the electrons and it is not frequency dependent. Therefore it is also called white noise. The root mean square value of the Johnson-Nyquist noise is given by [7]:

$$U_{\text{noise}}^{\text{rms}} = \sqrt{4k_{\text{B}}TR\Delta f}. \quad (3.19)$$

Here  $k_{\text{B}}$  is the Boltzmann constant,  $T$  the temperature,  $R$  the resistance and  $\Delta f$  is the bandwidth. For room temperature one can simplify this expression:

$$U_{\text{noise}}^{\text{rms}} = 0.127 \frac{\text{nV}}{\sqrt{\text{Hz}\sqrt{\Omega}}} \cdot \sqrt{R} \cdot \sqrt{\text{ENBW}}. \quad (3.20)$$

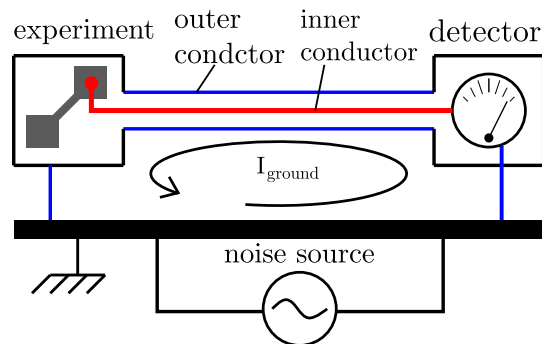
ENBW is the equivalent noise bandwidth of the low pass filter in the lock-in amplifier. If the low pass filter is chosen with a slope of 24 dB/oct the ENBW is  $5/(64T)$ , where  $T$  is the time constant. The important point here is that the noise depends on the resistance. Since we carry out our measurements at magnetic tunnel junctions, the resistance changes during the measurement because of the TMR effect. This could lead to a change in noise during the measurement misinterpreted as magneto-Seebeck effect.

### 3.3.2. Flicker noise

In contrast to Johnson-Nyquist noise, Flicker noise depends on the exact type of resistance. For example the Flicker noise of a carbon composition resistor is bigger than for a thin film like a tunnel junction. The power spectrum of the Flicker noise depends on the frequency. Thus it is also called  $1/f$  noise or pink noise. Because the power density drops for bigger frequencies, Flicker noise is not important in AC measurements with high frequency, in which white noise is dominant.

### 3.3.3. Ground loops

In the laboratory are many external noise sources like the air conditioning system or magnetic fields. However, most of these signals are asynchronous, so that the lock-in amplifier does not detect them. But there are also noise sources at the same frequency as the reference signal. Mostly they originate in the experiment itself. Especially ground loops can be a problem. An example for a ground loop is shown in figure 3.5. Here, both the experiment and



the detector are grounded to a reference ground. The detector measures the signal against this reference ground. Additionally, the experiment and the detector are connected via the outer conductor of the coax cable. So there is a shorted circuit. If there is any noise source, as sketched in figure 3.5, along this shorted circuit, the grounding potential at the experiment and at the detector are not equal. So there is a current in this circuit which influences the measurement.

**Figure 3.5.:** Ground loop in a simple measurement setup.

### 3.3.4. Shielded conductors

In our experiments only coax cables are used. These cables are shielded. Everything in the experiment should be shielded, otherwise currents are induced. To understand this, figure 3.6 can be considered. In the upper case the inner conductor has

### 3. Experimental setup

---

a charge  $Q_1$ . This causes an electrical field between the inner and outer conductor. So there is an induced charge of  $Q_2 = -Q_1$  at the outer cable because it is grounded. The important fact is that there is no electrical field outside of the coax cable and  $Q_3$  equals zero.

In the lower case, the shield is incomplete. As a consequence there is an external field. This induces a charge  $Q_3$  in the second conductor. The charge depends on the potential in the first conductor and the so called mutual capacitance  $c_{31}$ . The mutual capacitance is a function of the exact geometry:

$$Q_3 = c_{31} \cdot U_1 . \quad (3.21)$$

In the upper case  $c_{31}$  is zero and it is obvious that no charge is induced. If the mutual capacitance  $c_{1,\text{ground}}$  equals zero, the charge  $Q_1$  is given by  $|Q_2 + Q_3|$  in both cases.

Now, the more dangerous case of a non statical potential is considered. This would mean that the potential in the inner left conductor changes with time and thus also the charge because of the self-capacitance  $c_{11}$ :

$$Q_1(t) = c_{11} \cdot U_1(t) . \quad (3.22)$$

Again, because of the mutual capacitance  $c_{13}$ , a charge is induced in the right conductor

$$Q_3(t) = c_{13} \cdot U_1(t) . \quad (3.23)$$

Because the charge is not constant anymore, the derivative of the charge can be taken, which means there are currents in the conductors:

$$I_1 = \frac{dQ_1(t)}{dt} = c_{11} \cdot \frac{U_1(t)}{dt} , \quad I_3 = \frac{dQ_3(t)}{dt} = c_{13} \cdot \frac{U_1(t)}{dt} . \quad (3.24)$$

If the voltage in the conductor has the same frequency as the reference frequency

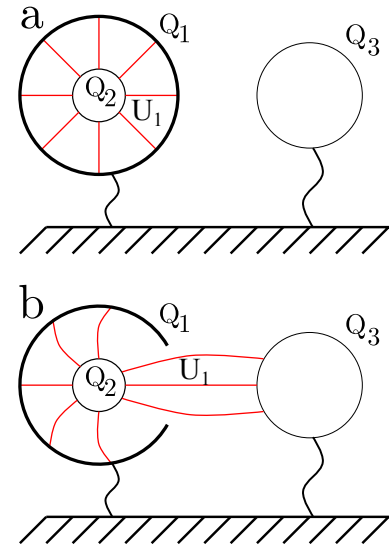


**Figure 3.6.:** Shielded and non shielded conductors.

( $U_1(t) = U_0 \cdot \sin(\omega_{\text{ref}} t)$ ), the current has also the same frequency but is phase shifted:

$$I_1(t) = c_{11} \cdot U_0 \cdot \sin\left(\omega_{\text{ref}} \cdot t + \frac{\pi}{2}\right), \quad I_3(t) = c_{13} \cdot U_0 \cdot \sin\left(\omega_{\text{ref}} \cdot t + \frac{\pi}{2}\right). \quad (3.25)$$

Thus, a lock in amplifier would detect signals with this frequency. A consequence is that a complete ground loop is not required to carry a current. The changing electrical field mediates the current flow. Additional vibrations - especially with the reference frequency - can be a problem. Here the geometry would change periodically and thus the mutual capacitance  $c_{13}$  would become time dependent. With a similar calculation as above one would see that there is a current.

### 3.3.5. The laboratory ground

As ground a heavy conductor should be used. Nevertheless it has a finite resistance and if one point is defined as the laboratory ground with zero potential, a nearby point could have a different potential. Another problem is that all electronic consumers are connected to the ground, including the measurement devices.

### 3.3.6. Proper grounding

It is very important to shield measurement signals and to ground this shield properly if parasitic signals should be prohibited. As an example the amplification circuit in

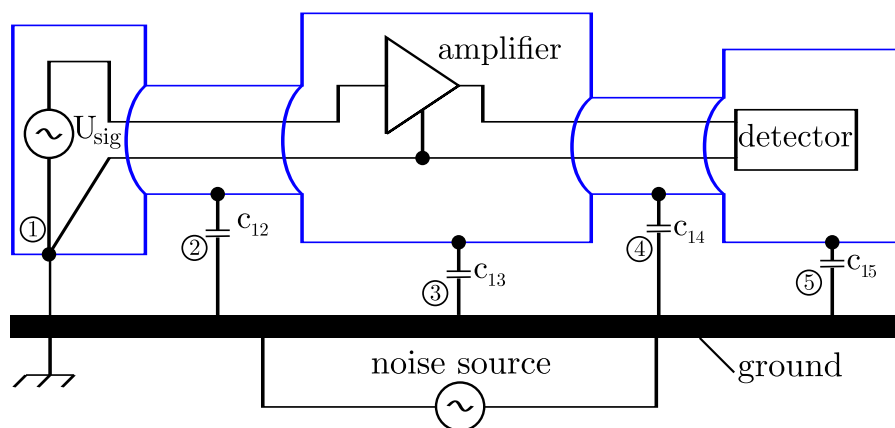


**Figure 3.7.:** Grounding the shield of an amplifier properly [10, p. 37].

figure 3.7 is considered. Here two-conductor shielded wires are used. This means, there are two conductors in the shield. One of these conductors carries a signal from the experiment through an amplifier into the detector. The other conductor carries the reference signal. The shield is drawn in blue.

To prevent noise in the measurement two rules are proposed by Morrison [10, page 33-48]:

- It is important to connect the shield to the zero reference potential (point 1, figure 3.7). Otherwise it would be possible that noisy signals from the ground are induced in the shield via mutual capacitances (like  $c_{13}$  or  $c_{14}$  in figure 3.7) and then these signals are induced in the reference conductor again via mutual capacitances. This could lead to a shorted circuit because the reference conductor is also grounded (at point 1). The circuit is closed over the ground connector. Of course there is only sense in grounding the shield, if the reference signal is grounded, too.
- The shield has to be grounded at the same point as the reference signal (point 1). Otherwise a shorted circuit could arise again if there is a noise source at the ground. This time, the current would be induced to the shield via mutual capacitances (eg.  $c_{14}$  or  $c_{15}$ ) and while the shield is connected to the reference conductor, the current would flow through the reference cable to the reference ground point and back via the ground conductor. In summary it is necessary that the currents induced in the shield can drain to the reference ground connection.

## 3.4. Experimental setup

### Flow chart of the setup

The magneto-Seebeck effect occurs in magnetic tunnel junctions (MTJ) with a temperature gradient. A temperature gradient will cause a Seebeck voltage which depends on the relative magnetic alignment of the two ferromagnetic layers in the MTJ. In this experiment, the general idea is to generate the temperature gradient with a laser and measure the Seebeck voltage with a lock-in amplifier. To change the external magnetic field an electromagnet is used.

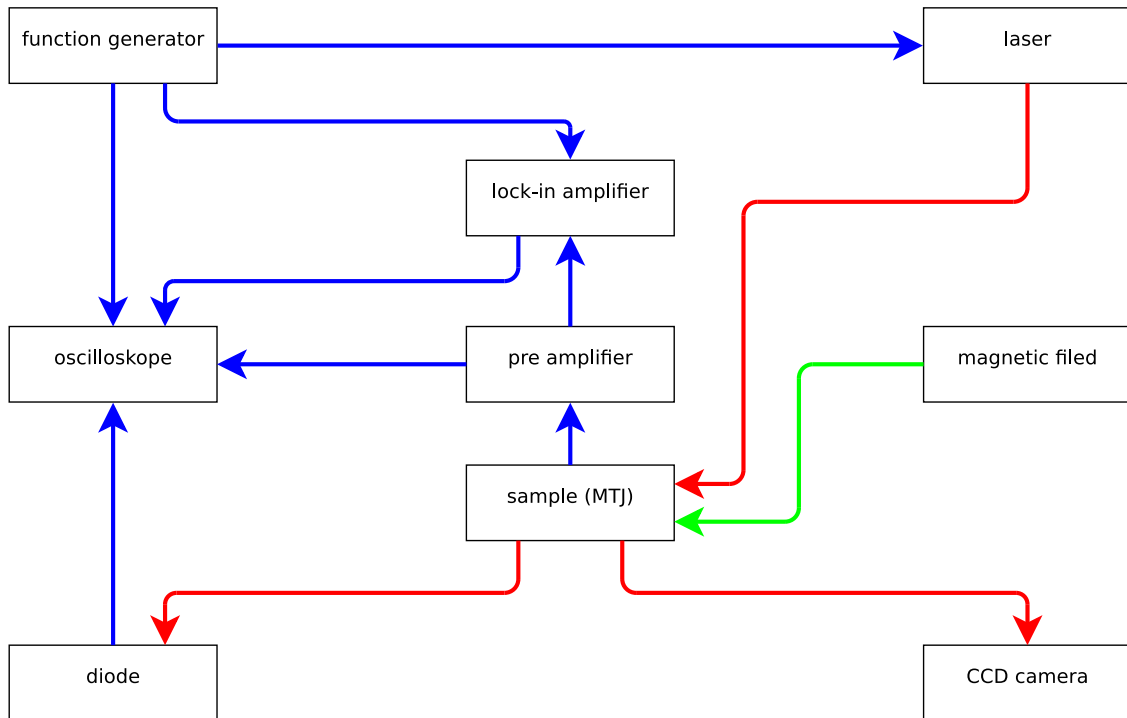


**Figure 3.8.:** Basic experimental setup represented in a flowchart. Blue lines indicate electrical signals, red lines laser light and the green line marks a magnetic signal.

The setup is drawn in figure 3.8 as a flowchart. First, a function generator is used to modulate the laser signal (which is a requirement to use a lock-in amplifier). The laser is modulated with a rectangular function between 0 V and +5 V and a frequency of 1.5 kHz. As a result, there is light for 333  $\mu$ s and after that the laser is off for the same time. Besides, the signal of the function generator is also used as reference signal for the lock-in amplifier and as trigger signal for the oscilloscope. As mentioned above, the laser heats the sample which causes a Seebeck voltage. The sample is electrically contacted with thin gold wires, so that a voltage can be tapped and amplified with a pre-amplifier. The pre-amplified voltage can either be seen in the oscilloscope or measured with the lock-in amplifier. The lock-in amplifier has a monitor out channel to display the input signal on the oscilloscope after the lock-in amplifier has amplified but not filtered it.

The sample does not absorb the whole laser light but reflects a huge amount. This reflected light is measured with a fast diode and a CCD-camera. The camera is

used to position the MTJs exactly below the laser spot. The diode detects the light and displays its intensity on the oscilloscope. So it can be used to check the laser signal. Additionally, the diode is used to determine the beam waist.

### 3.4.1. Beam path

In general, there are two possibilities to generate a temperature gradient which is necessary to measure the magneto-Seebeck effect  $S_{MS}$ . The first one is resistive heating. Here, a current is used to heat small wires on the top or at the bottom of the tunnel junction.

In this work a diode laser is used to generate a temperature gradient along the tunnel junction. The beam path is outlined in figure 3.9. First, the laser beam passes the lenses  $L_1$  and  $L_2$ . The lenses are arranged as a Kepler telescope, so they reduce the diameter of the beam spot. After the Kepler telescope, the beam passes a beam splitter  $B_1$ . In the ideal case 100% should be transmitted, so there is no energy loss in reflection. The beam is then focused with a microscope-objective on the sample to the size of a tunnel junction. The diameter of the beam is roughly  $10\ \mu\text{m}$ . The beam hits the sample perpendicular to its surface.

Afterwards, the beam is reflected back from the sample. But this time, the beam is reflected at the beam splitter  $B_1$ . Thus, it passes the lens  $L_3$  and is focused via another beam splitter  $B_2$  on a fast photo-diode and on a CCD camera. One can quantify with the diode the intensity of the reflected light at the sample time resolved. In this experiment the diode is also necessary to determine the beam waist.

The part of the beam path with the CCD camera works as a confocal microscope.

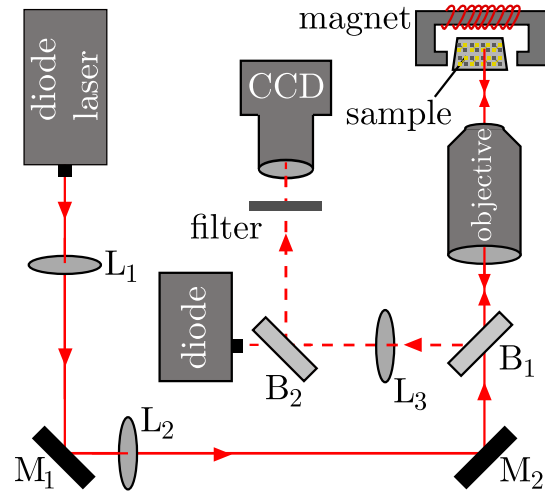


**Figure 3.9.:** Beam path to heat the sample with a laser spot.

The confocal microscope is essential to place the sample at the right position, because it is important to hit exactly the tunnel junction with the laser spot.

A magnetic field of up to 50 mT can be applied to the sample with an electromagnet, also shown in figure 3.9.

### 3.5. Laser intensity

To calculate the intensity of the laser light, used for heating, the beam waist must be measured. Unfortunately, there is no unique definition of the beam waist. For example in case of a Gaussian beam the  $1\sigma$ -environment can be used as beam waist as well as the  $2\sigma$ -environment. However, in the thesis the  $2\sigma$ -environment is used as beam waist.

To measure the beam waist the *knife edge method* is used. This method is explained in detail in the appendix. The basic idea is to move a sample perpendicular to the laser beam so that the beam hits areas with different reflectivity. The intensity of the light is measured. The recorded data points can be fitted to an error function:

$$P = a + b \cdot \operatorname{erf} \left( \frac{\sqrt{2}(x - x_0)}{\omega_x} \right). \quad (3.26)$$

Here  $\omega_x$  is the beam waist.

In the experiment, the power of the whole laser beam is measured. However, in the area given by  $\omega_x$ , as determined by equation (3.26), approx 91% of the measured power are deposited. This factor is considered by calculation the intensity. For the simulation later in this work, this factor is of no importance, since the Gaussian beam profile is considered. For more details see section A in the appendix.

### 3.6. TMR measurement

It is also important to determine the TMR ratio of the tunnel junctions used for TMS measurements. To perform this measurement, a Keithley 2400 source meter is used. A bias voltage of 0.01 V is applied to the MTJ and the current is measured. Thus, the resistance can be calculated. Additionally, an external magnetic field is applied. With this field it is possible to change the alignment of the ferromagnetic

layers. So the resistance is measured as a function of the external magnetic field. With equation (2.6) the TMR ratio can be calculated.

### 3.7. Wire bonder

The magnetic tunnel junctions can be contacted with small gold wires via bond pads. To contact the bond pads with the gold wire, a wire bonder is used. The general idea is that the wire is pressed on the bond pad and melted by ultrasound. Thus the wire and the bond pad are electrically connected.

For best results, gold wire is used for bonding on gold bond pads. The bonding process can be influenced with four parameters:

- The bonding power is the amount of power applied to the wire. High power means a high ultrasonic amplitude.
- The bonding time. This is the time, the ultrasonic signal is applied to the bonding wire.
- The force that is used to press the bonding wire onto the sample.
- The sample holder can be heated.

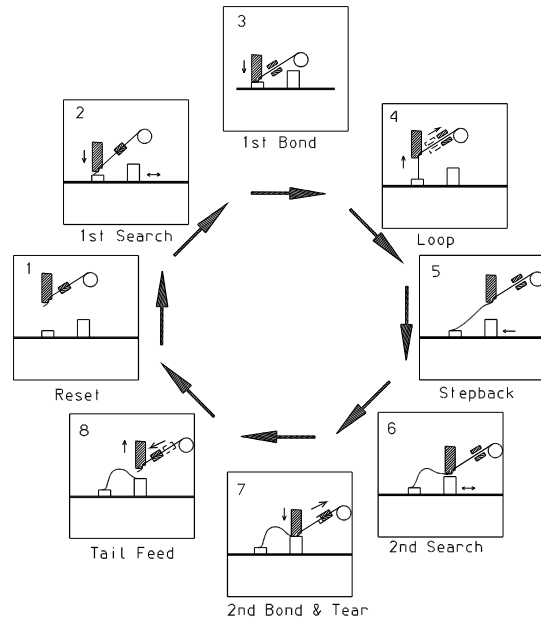


**Figure 3.10.:** Work cycle of the wire bonder. [12]

If some parameters are too low, there is no good contact between bond pad and wire. On the other hand, if the parameters are chosen too high, the junction may break.

The work cycle of the wire bonder is shown in figure 3.10. The bonding wire is threaded through a small hole in the bonding wedge. Starting with the first picture in figure 3.10, the bonder is in the reset position. In the second step, the wedge has to be placed over the right bonding position. Here, the wedge can be lowered to the bond pad and the position can be corrected before the wedge touches the

bond pad. When the bond pad is touched, the ultrasonic pulse is applied to the wire and the first bond is made (step 3). Afterwards the wedge can be raised again. The sample is moved so that the bonding wedge is over the next bonding position (step 4 and 5). Now again the ultrasonic vibration can be applied to make the next contact and the wire is teared.

### 3. *Experimental setup*

---

# 4. Experimental results

## 4.1. General approach

In this section various experimental results will be presented and discussed. As explained in section 3.4 the Magneto-Seebeck effect shall be measured. Therefore a laser is used to heat a magnetic tunnel junction. Different measurements have to be performed. The general approach contains five steps, as follows:

- Determine the TMR ratio of each MTJ.
- Measure the TMS effect as a function of the laser power.
- Measure the TMS effect as a function of the laser position.
- Record oscilloscope traces of the thermo-voltage.
- Perform measurements for different barrier sizes.

The TMR ratio is measured to estimate the quality of the tunnel junctions. As mentioned before, the TMR and the TMS effect are not related to each other. Thus a high TMR ratio does not mean a high Magneto-Seebeck effect. But if a junction has a high TMR ratio, the quality of the junction can be assumed to be good and so the element may have a good TMS ratio.

The TMS effect is measured as a function of the laser power. Theoretically, a sign change of the Magneto-Seebeck effect as a function of the laser power was predicted for special structures of the ferromagnetic layers (see section 2.4). This theory will be verified.

As finite element calculations with Comsol Multiphysics show, temperature gradients just occur where the laser spot hits the sample. So one would expect to detect no voltage if the laser spot hits the sample somewhere else but not on the MTJ.

Nevertheless we detect thermo voltages even if the sample is heated somewhere else. Consequently, it is important to measure the TMS effect as a function of the laser position to determine whether there are other effects.

The thermo-voltage is also measured time dependent. These measurements are important to determine the origin of the voltages.

All these measurements were performed on samples with different MgO barrier thicknesses, because it is not clear which influence the MgO barrier has. Additionally the laser intensity has to be determined. Therefore the beam waist is measured.

## 4.2. Laser power

The laser power can be controlled by a software. However, the power applied to the sample differs from the power chosen in the software, because there are losses

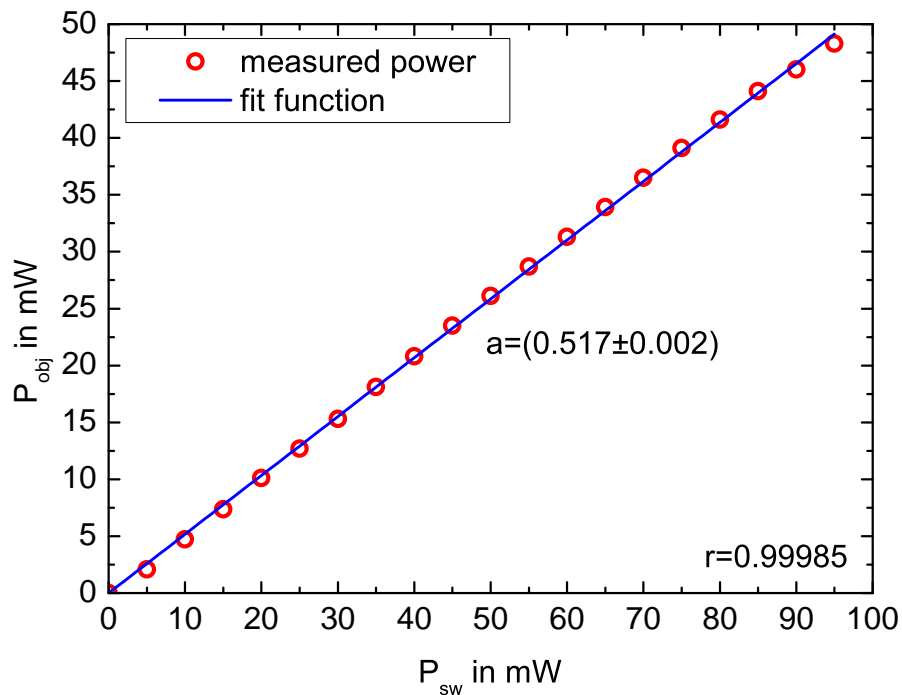


**Figure 4.1.:** Power dependence between applied power  $P_{obj}$  and chosen power  $P_{sw}$  in the software.

along the beam path. For example some light gets reflected by the lenses. Further, not all the light can pass the beam splitter  $B_1$  (see figure 3.9), because this beam splitter is especially suitable for light with a longer wavelength. Therefore, the power was measured directly in front of the objective. In figure 4.1, the power in front of the objective  $P_{\text{obj}}$  is plotted against the power chosen in the software  $P_{\text{sw}}$ . It is obvious that there is a linear correlation between the two parameters. The slope of the fitting curve is  $a = (0.517 \pm 0.002)$ . With this factor it is possible to calculate the power applied to the sample.

### 4.3. Beam waist measurements

For the beam waist measurement the sample is moved with a certain step size with respect to the laser beam. The change of reflectivity between a gold bond pad and the surrounding insulator is used to perform the measurement. The edge

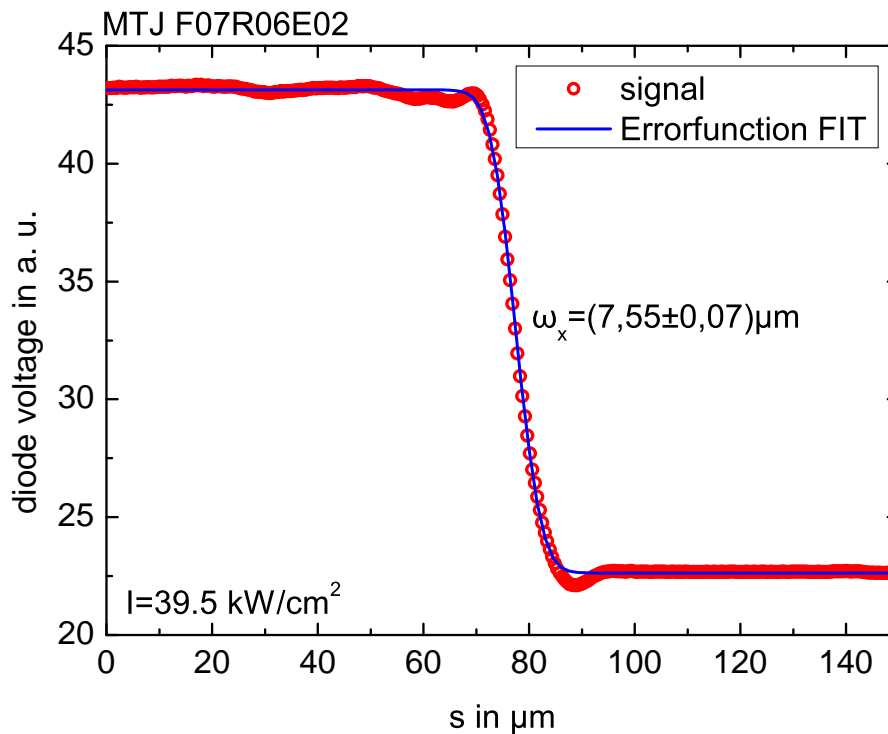


**Figure 4.2.:** Beam waist measurement on the sample vd120111-1.5. The measured data point and the fit function are shown.

#### 4. Experimental results

---

can be assumed to be sharp compared to the beam waist and is perpendicular to the direction of movement. An error function (equation 3.26) can be fitted to the measured points (figure 4.2). The measurement shown here was performed on the sample vd120111-1.5 at the MTJ F07R06E02, which has a 1.5 nm MgO barrier. From this error function, one obtains the beam waist, defined as the  $1/e^2$  radius of the Gaussian beam:  $\omega_x = (7.55 \pm 0.07) \mu\text{m}$ . Figure 4.2 shows that the error function fits very well to the measured data points. In general, the beam waist is measured for every MTJ separately to have a higher precision for the calculated intensity.

For this measurement the power in the software was chosen as  $P_{\text{sw}} = 100\text{mW}$ . Thus, the intensity can be calculated with:

$$I_{\text{avg}} = \frac{0.9111 \cdot 0.517 \cdot P_{\text{sw}}}{\pi \cdot \omega_x^2} = 26.3 \frac{\text{kW}}{\text{cm}^2} . \quad (4.1)$$

So the average intensity the sample vd120111-1.5 is exposed to is  $26.3 \text{ kW}/\mu\text{cm}^2$ , if the laser is set to 100 mW by the software.

## 4.4. Dependence on the insulator thickness

### 4.4.1. The investigated samples

To determine the influence of the insulator barrier thickness, a series of three different samples has been investigated, which differs only in the thickness of the MgO layer. The sample structure is drawn in figure 4.3. As substrate, silicon is used. The surface of the silicon is thermally oxidized. On the substrate, layers of tantalum and ruthenium are grown. The tantalum is used as a bottom contact. Above, there is the first layer of CoFeB, which is the first ferromagnetic electrode. It is followed by the MgO insulator, the thickness of the MgO is varied from 1.5 nm to 2.1 nm. On top of the insulator, there is the second ferromagnetic CoFeB layer. Next, there are two more tantalum and ruthenium layers and at last there is gold on top, used as the top contact. The general procedure will be to discuss all measurements which have been taken with one generic example for each barrier thickness.

### 4.4.2. TMR measurement

As mentioned above, first the TMR effect is measured to determine the quality of the tunnel junctions. The results are plotted in figure 4.4. For the recording of the data, the magnetic field has been varied in steps of  $\Delta B = 0.2$  mT. A bias voltage of 0.01 V was applied.

In figures 4.4(a) to 4.4(c) typical TMR curves can be seen. For the antiparallel alignment there is a higher resistance as for parallel alignment. Since none of the ferromagnetic layers are pinned, two switching events occur. Additionally, one can see in the TMR curves that the junctions do not switch very good because at  $B=0$  there is not a real parallel state. The layer with the smaller coercive field does not



**Figure 4.3.:** Stack structure of the sample vd120111-x.

#### 4. Experimental results

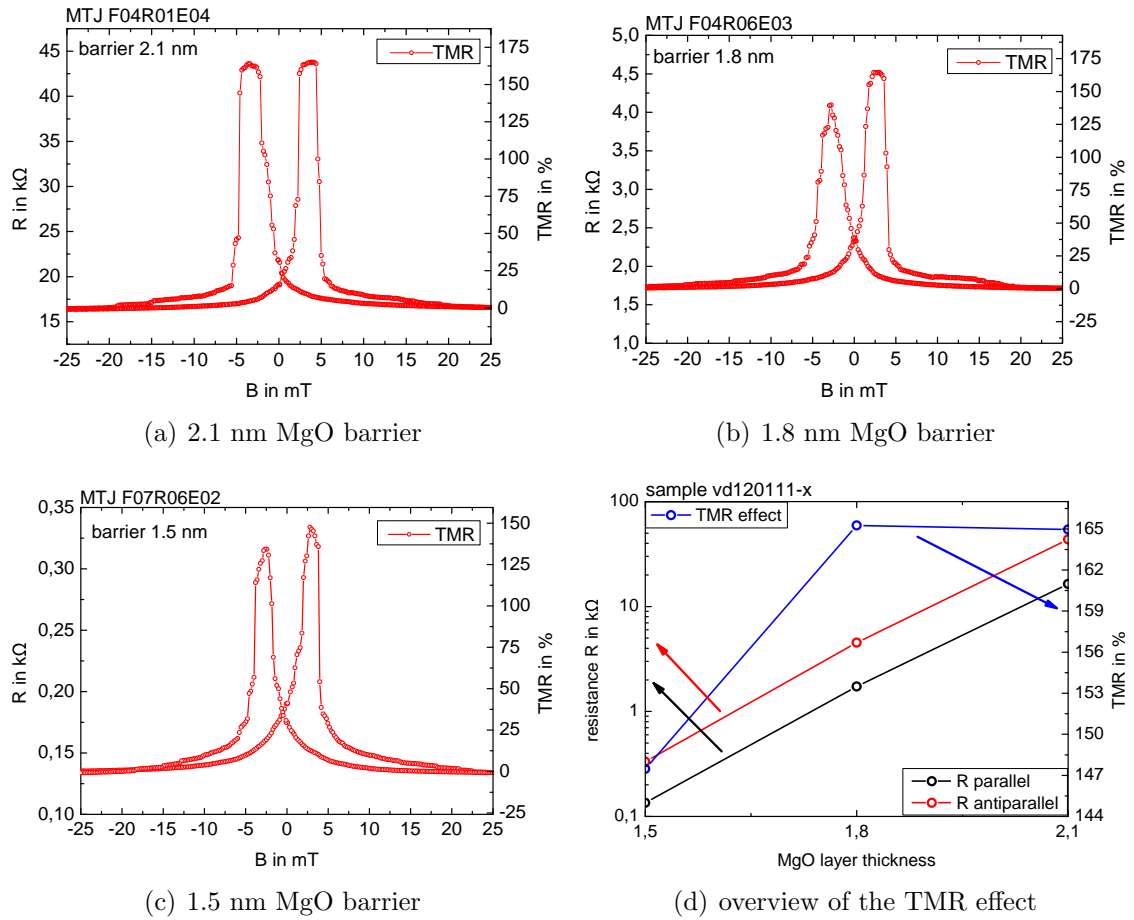


**Figure 4.4.:** TMR measurements on the sample vd120111-1.2.

seem to switch very abruptly. Further, some step like features can be identified which might be explained by several domains switching one after the other. The flanks would be very steep in the ideal case.

To get a more quantitative overview, the resistance for parallel and antiparallel alignment and the TMR effect is plotted as a function of the barrier thickness in figure 4.4(d). For the resistance a logarithmic scale was chosen. As explained in section 2.1, the tunnel current depends exponentially on the barrier thickness. Thus, also the resistance depends exponentially on the barrier thickness. This exponential dependence can be confirmed with the plot in figure 4.4(d).

The TMS effect varies between 145% and 165%. But there seems to be no dependence between barrier thickness and TMR effect.

## 4.4.3. TMS effect in detail

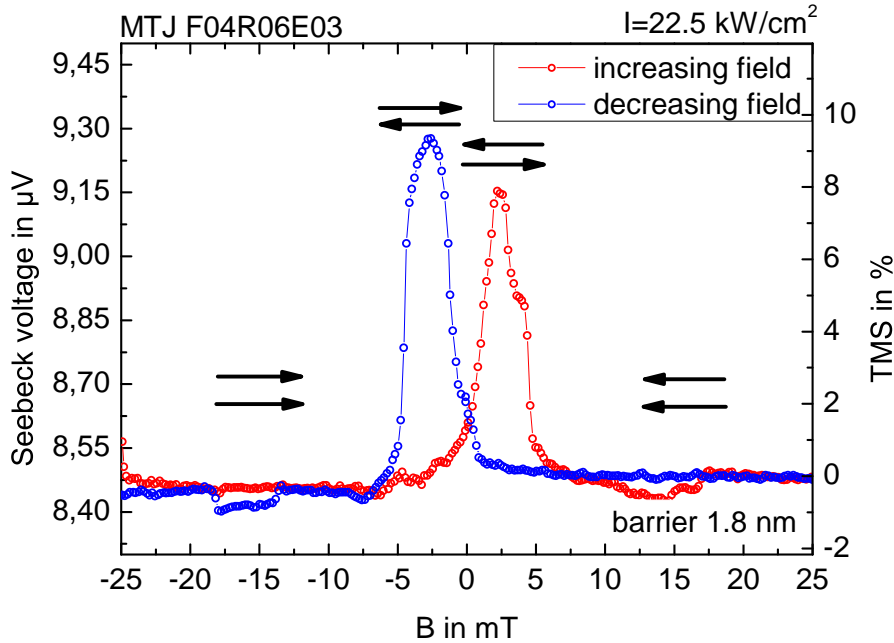


**Figure 4.5.:** TMS measurement of the MTJ vd120111-1.8-F04R06E03. The red dots highlight the part of the measurement with increasing magnetic field and the blue dots with decreasing magnetic field.

In figure 4.5, a TMS measurement is plotted in detail. The data points are the average values of two measurements that have been performed on this MTJ successively. At the beginning the magnetic field is set to  $-25$  mT. In this magnetic field both ferromagnetic layer are aligned in the same direction. Afterwards, the field is increased in steps of  $\Delta B = 0.2$  mT (red line in figure 4.5). Until  $0$  mT is reached, no change in the magnetic alignment should take place. If the magnetic field is increased further, one magnetic layer changes its direction first, because it has a smaller coercive field, and the two ferromagnetic layers are aligned antiparallel. This leads to a higher Seebeck voltage because of the Magneto-Seebeck effect. For more than  $5$  mT the second layer is switched entirely, too. Consequently, there is again a state of parallel alignment and a smaller Seebeck Voltage is measured. Both ferromagnetic layers are pointing in the other direction now.

The same applies for the other field sweep direction. The alignment of the layers in each state is marked with arrows in figure 24.

#### 4.4.4. Power dependence of the TMS effect

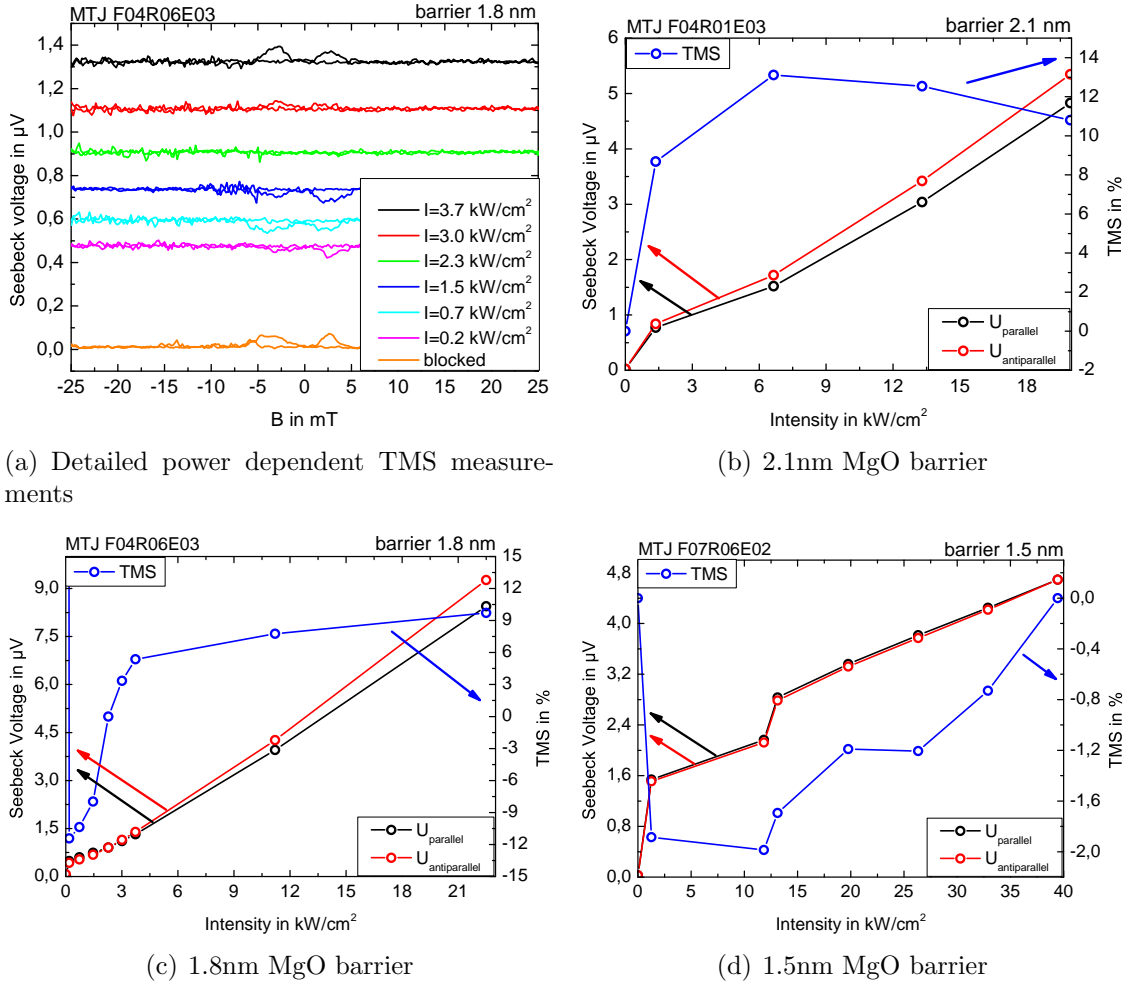


**Figure 4.6.:** Seebeck voltages for parallel and antiparallel alignment are plotted on the left axis as a function of the applied laser power. On the right axis the TMS effect is plotted against the applied laser power.

Now the power dependence of the TMS effect shall be investigated for all three barrier thicknesses. TMS measurements for several intensities, as described in the previous section, have been performed on the different samples. As an example, the measurements performed on the MTJ with 1.8 nm MgO barrier are shown in figure 4.6(a). The plotted intensities are in an interval between no intensity and  $I = 3.7 \text{ kW}/\text{cm}^2$ . For every intensity the typical TMS curve is plotted (Seebeck voltage against applied magnetic field). It can be seen clearly that the offset for

the TMS curves increases with the intensity. This means there are higher Seebeck voltages in case of higher laser intensities. This is plausible because higher laser intensities lead to a higher temperature gradient. But not only the Seebeck voltage changes with the intensity, also the Magneto-Seebeck effect: For an intensity of  $I = 3.7 \text{ kW/cm}^2$  the Seebeck voltage for antiparallel alignment is bigger than for parallel alignment. This means a positive magneto-Seebeck effect.

In case of  $I = 2.3 \text{ kW/cm}^2$ , there are no peaks and so there is no Magneto-Seebeck effect.

If the intensities are smaller, like at  $I = 1.5 \text{ kW/cm}^2$ , the Seebeck voltage decreases in the antiparallel states. Here, the magneto-Seebeck effect is negative.

There is also a big problem in the measurement shown in figure 4.6(a): When the laser is blocked, there is still an effect visible. Of course this cannot be the magneto-Seebeck effect since there cannot be a temperature gradient without laser heating and as a result no Seebeck voltage. For parallel alignment the voltage is really small. The origin of this small voltages are thermal fluctuations. Whereas in the state of antiparallel alignment the voltage is much bigger and cannot be explained to this extent with thermal fluctuations of the higher resistance in the antiparallel state. The origin of the higher voltages are probably noise sources like a ground loop.

In figures 4.6(b) to 4.6(d) the voltage in parallel and antiparallel state as a function of the intensity is plotted on the left axis and the TMS effect as a function of the intensity on the right axis.

For a barrier of 2.1 nm (figure 4.6(b)), the Seebeck voltage is increasing with increasing intensity. If the laser is blocked, there is no magneto-Seebeck effect at all and a very small voltage signal. When the junction is heated by the laser, a magneto-Seebeck effect of about 10% can be measured. A dependence between intensity and magneto-Seebeck effect is not discernible. It seems rather that the TMS effect remains constant and fluctuates around an average value. The TMS effect is overall positive.

The TMS effect for junctions with 1.8 nm MgO barrier has already been discussed (figure 4.6(a)). In figure 4.6(c) the quantitative progression of the TMS effect as a function of the intensity is plotted. First, the TMS effect is increasing fast but for intensities bigger than  $3.7 \text{ kW/cm}^2$  the TMS effect nearly remains constant. In contrast to the sample with 2.1 nm MgO barrier, the TMS effect is negative for low

intensities, has a sign change at an intensity of  $I \approx 2.3 \text{ kW/cm}^2$  and is positive for higher intensities.

The thinnest investigated barrier is 1.5 nm thick (figure 4.6(d)). Again the Seebeck voltage increases with increasing laser intensities. By looking at the TMS values, one ascertains that there is no TMS effect if the laser is blocked. Also in this case the TMS effect increases with increasing laser power. The interesting thing is that the TMS effect is negative for all applied laser intensities. For the highest intensity, the magneto-Seebeck effect reaches zero. Thus one could assume that the effect would become positive, if the intensity is increased further.

In summary: For the thinnest MgO barrier of 1.5 nm MgO the Magneto-Seebeck effect is always negative. For 1.8 nm barrier thickness a sign change occurs at intensities of  $I = 2.3 \text{ kW/cm}^2$ . In case of the thickest barriers of 2.1 nm MgO, the TMS effect is positive for all measured intensities. Only for the sample with 1.8 nm barrier the problem occurred that there is a TMS like effect, when the laser is blocked. A reason for this problem could be ground loops.

#### 4.4.5. Time resolved Seebeck signal

For each measured intensity also the oscilloscope traces have been recorded (figure 4.7). They show how the Seebeck voltage, induced by the laser, changes with time. In general, the oscilloscope traces for all samples look similar. At about 0.2 ms there is a negative peak. This is the time when the laser starts heating the sample. The peak depends on the intensity of the laser light applied to the tunnel junction. After the peak a plateau follows which depends on the laser intensity and also on the sample. There is a second peak, this time positive when the laser stops heating the sample. Beyond this peak the signal reaches the zero voltage line again and is in its initial state, as before the laser pulse has arrived.

In figure 4.7(a) the signal for blocked laser is superimposed by an oscillation. The frequency of this oscillation is around 71 kHz. After these measurements it was possible to identify the power adapter of the CCD camera as noise source. So it is possible to eliminate this source of noise.

As mentioned above, there are two contributions to the oscilloscope signal: The peaks and the plateaus. The peaks may belong to a temperature gradient that is only present when the laser is switched on or off and the plateaus belong to a static

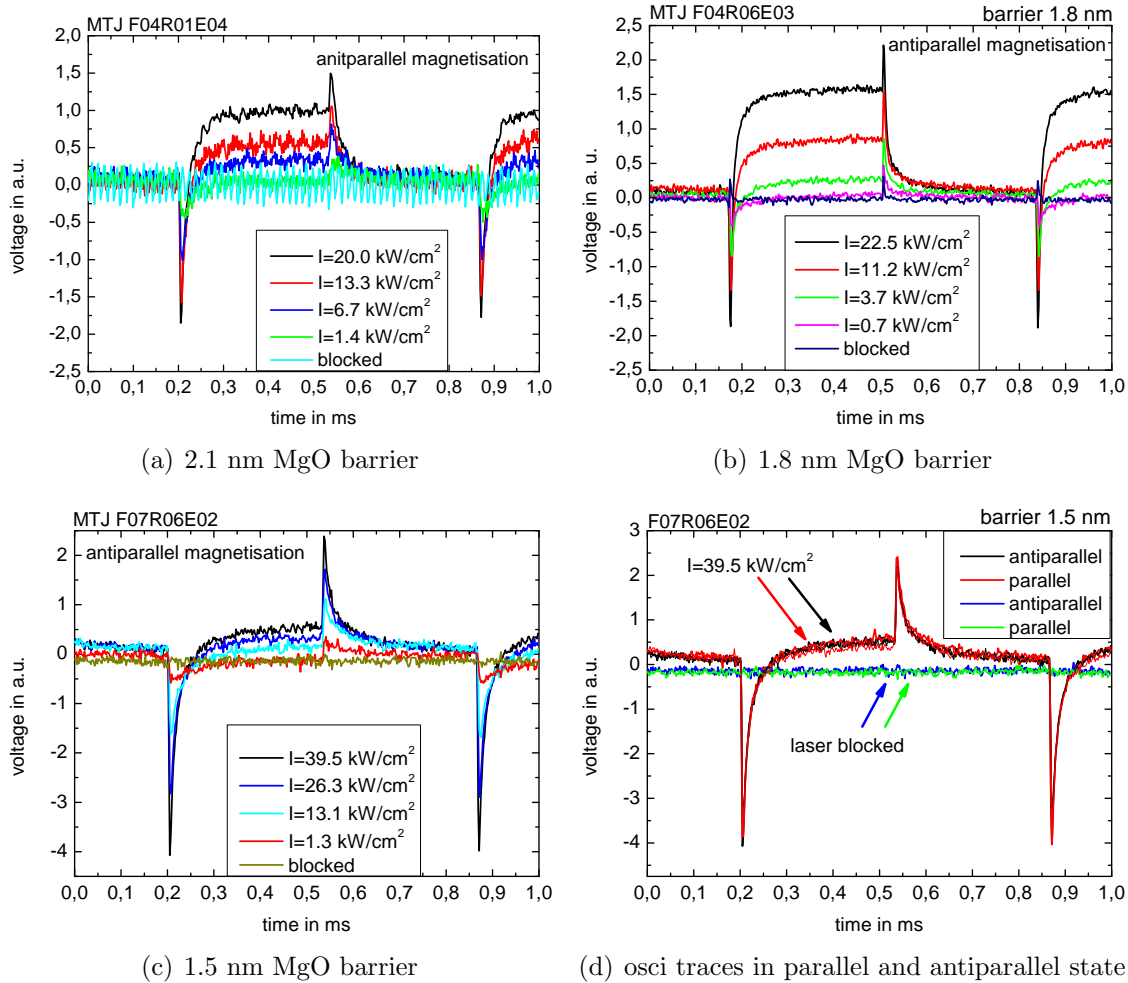


**Figure 4.7.:** Seebeck voltage as a function of the time. The laser is modulated with 1.5 kHz and the oscilloscope is triggered with this reference frequency.

gradient that does not vary with time. Right after the peak there is an exponential decay of the signal. This is especially good noticeable at the time when the laser is switched off.

Still, there is the question of the origin of these signals. The rectangular signals should be a Seebeck voltage and thus lead to the magneto-Seebeck effect. To understand the peaks it has to be considered that tunnel junctions are capacitors in which the MgO barrier is the dielectric. So the exponential like decay can be explained by a discharging capacitor. It is possible to determine the time constant with a fit. The discharging process is described with the following equation:

#### 4. Experimental results

$$U(t) = U_0 \cdot e^{-\frac{t}{\tau}} + U_{\text{Offset}} . \quad (4.2)$$

$U(t)$  is fitted to the exponential decay to determine the time constant (see figure 4.8). Both time constants for parallel and antiparallel magnetization can be seen in the figures. The capacitance on a RC-circle can be calculated if the time constant is known:

$$C = \frac{\tau}{R} \Rightarrow C_P = (490 \pm 20)\text{pF}, \quad C_{\text{AP}} = (1110 \pm 90)\text{pF} . \quad (4.3)$$

The resistance is known from the TMR measurement (figure 4.4). In equation 4.3 just the error from the fit has been taken into account. In the simple model with the tunnel junction as a capacitor the capacitance should not change, if the alignment of the magnetic electrodes changes. One explanation would be that the Seebeck signal is not rectangular but has also flanks where the voltage increases and decreases exponentially, so that two processes are superimposed.

However, there is a second possibility to calculate the capacitance of a tunnel junction by assuming a parallel plate capacitor:

$$C = \epsilon_0 \epsilon_r \frac{A}{d} = 2.3 \text{ pF} , \quad (4.4)$$

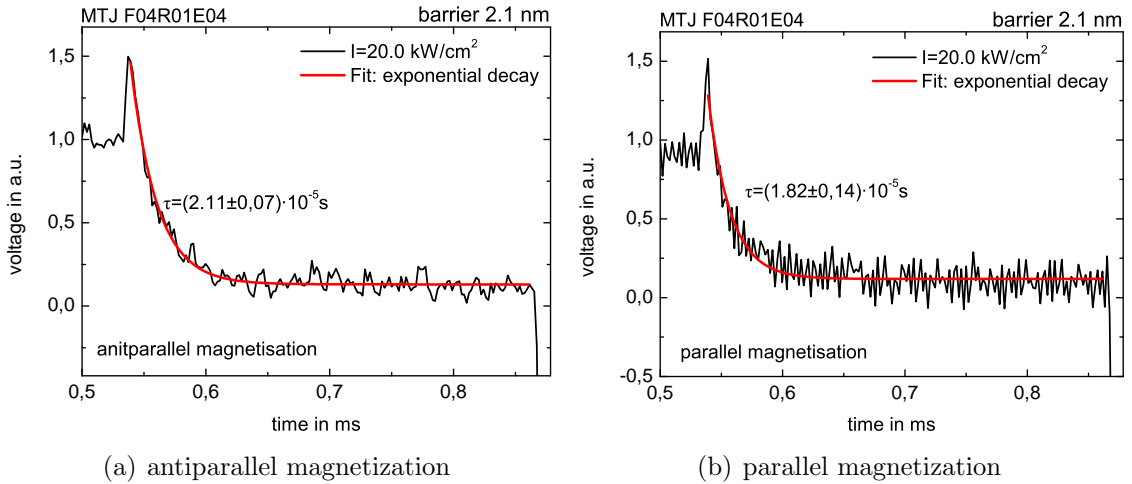


**Figure 4.8.:** Detailed extract of the oscilloscope traces to visualize the exponential fit.

where  $A$  is the area of the tunnel junction ( $7.5\ \mu\text{m} \cdot 7.5\ \mu\text{m}$ ) and  $d$  the distance between the electrodes (2.1 nm). The relative permittivity<sup>1</sup> of MgO is  $\epsilon_r = 9.65$ . The capacitance calculated in this way is two orders of magnitude smaller. Anyway, another capacitance can be considered: The gold bond pad acting as one electrode, the metal layers covering the whole substrate as the other, with the oxide surrounding the junction as dielectric. The total area of the electrodes is assumed to be  $0.045\ \text{mm}^2$  and the distance between the two electrodes 64.5 nm, the capacitance will be  $C = 60\ \text{pF}$ . This capacitance is more plausible and shows, that capacitive effects should be considered by explaining the signal. Additionally, the substrate can have an influence on the capacitances. This will be discussed later in section 4.5.6.

Figure 4.7(d) shows the differences in the oscilloscope traces for parallel and antiparallel magnetization for a high intensity and no intensity. In both cases there are no obvious differences. Just the fits with an exponential function (figure 4.8) show that there are indeed differences.

#### 4.4.6. Position dependence of the TMS effect

It is important to investigate the position dependence. From simulations one would expect that the sample is heated just directly where the laser hits the sample. So in an ideal case there would not be any voltage if the sample is heated somewhere else, like on the substrate or on the MTJ next to the contacted MTJ. However, voltages have also been measured when the sample was heated somewhere else.

The position dependent TMS measurements are plotted in figure 4.9. For measurements of the samples with 2.1 nm and 1.8 nm MgO, the voltage is smallest, if the next MTJ is heated. This is the measurement with the biggest distance between heating point and contacted MTJ.

First, the sample with 2.1 nm MgO barrier is considered. If the laser heats the insulator, the Seebeck voltage increases. Whereas the magneto-Seebeck effect decreases. When the laser heats the next MTJ there is still a small effect but the voltage is a factor of 2 smaller.

For the 1.8 nm barrier the voltage gets much smaller for both measurements: heating on the insulator and heating on the next element. But there is still a magneto-

---

<sup>1</sup><http://www.korth.de/index.php/material-detailansicht/items/22.html>, 12/07/19

#### 4. Experimental results

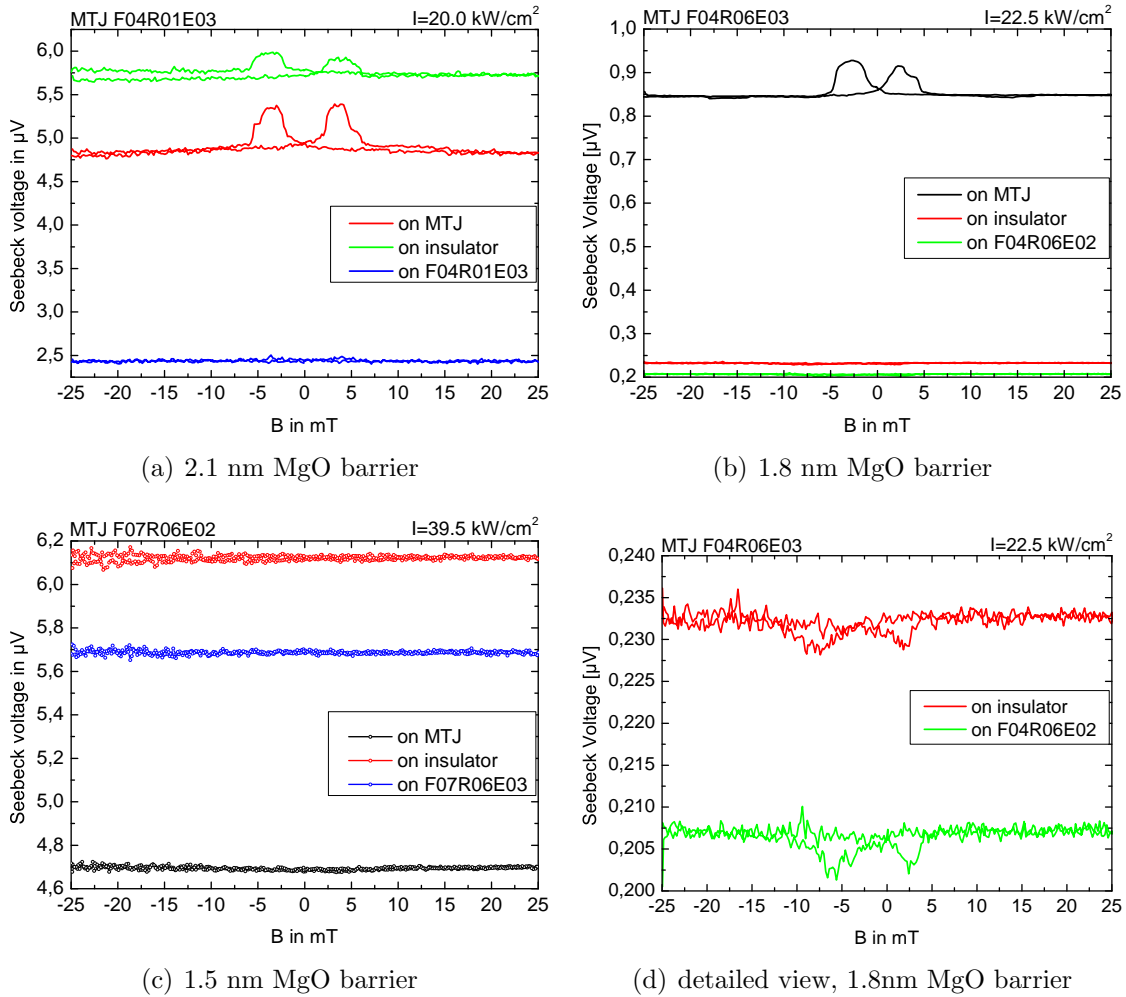


**Figure 4.9.:** Position dependence of the TMS signal.

Seebeck effect with the opposite sign as if the laser heats the junction.

In case of the thinnest barrier (1.5 nm) the voltage increases also when the insulator is heated. For all applied thermo voltages there is no TMS effect visible.

A trend can be observed that the sign in the position dependent measurement changes if there is a change in the power dependent measurement and vice versa.

#### 4.4.7. Position dependence - time resolved

The oscilloscope traces of the position dependent measurements are shown in figure 4.10. In figure 4.10(a) the voltage is positive, if the laser heats the junction. When

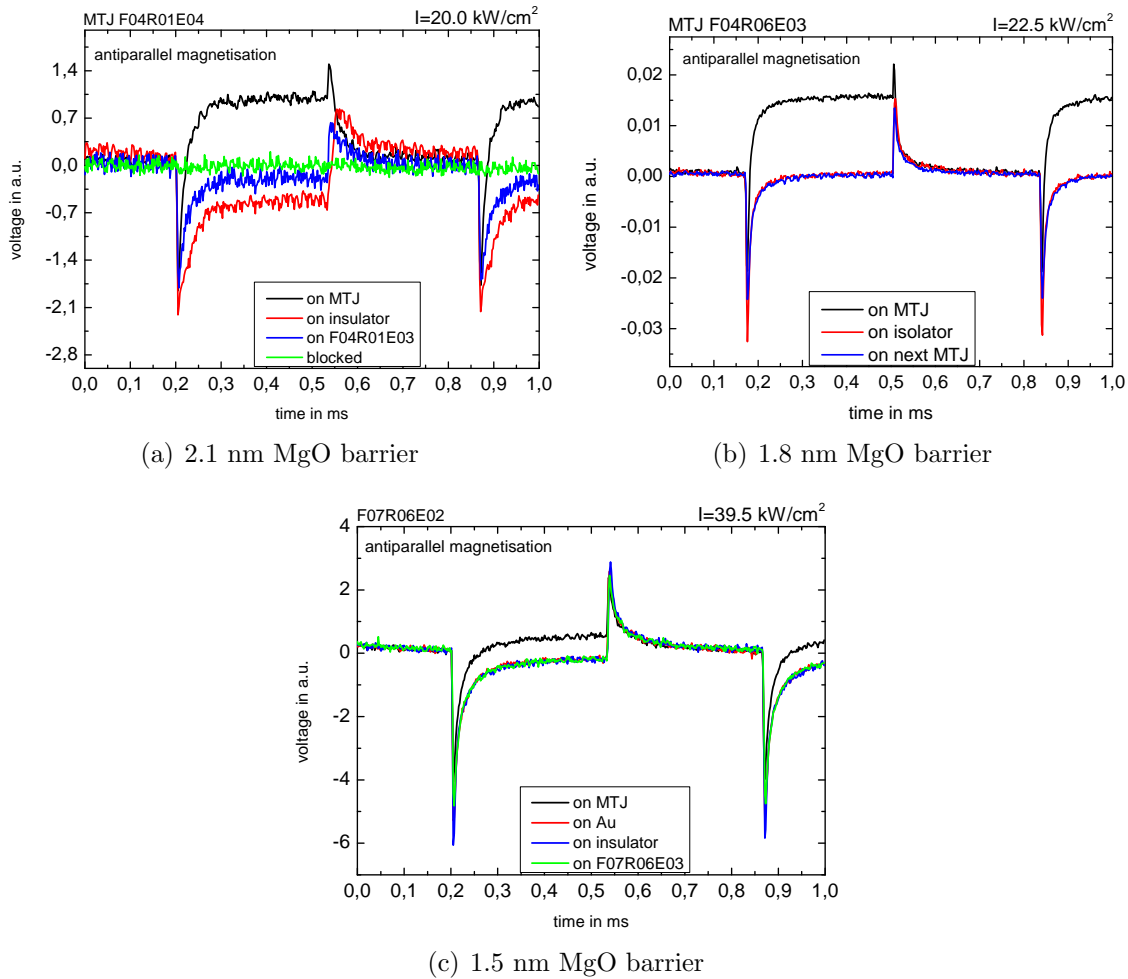


**Figure 4.10.:** Oscilloscope traces for different positions of the laser spot on the sample.

the laser heats on the insulator or the next element the voltage gets negative. Of course this can not be seen in figure 4.9(a), because the lock-in amplifier detects just the absolute value of the voltage. In the second and third graph (figure 4.10(b) and 4.9(c)) again a small negative signal is noticeable when the insulator or the next junction is heated.

These measurements can be used to estimate the influence of the peaks in the lock-in signal. In general, peaks should have a small influence. They can be represented with a  $\delta$ -function that converges badly in a Fourier series. In fact, if figure 4.10(b) is considered, one can see big peaks when the laser heats the insulator or the next

#### 4. *Experimental results*

---

junction. But the voltage detected by the lock in (figure 4.9(b)) is much smaller in comparison to the rectangular like signal measured with laser spot on the tunnel junction. As a conclusion, the peaks have a much smaller influence on the magneto-Seebeck measurement performed with the lock-in as the rectangular signal. The position dependent oscilloscope traces will be discussed in more detail for the sample with exchange bias.

## 4.5. Sample with exchange bias

A sample with exchange bias has also been investigated. Exchange bias means that one layer is pinned. A ferromagnetic layer can be pinned by using an antiferromagnet. The antiferromagnet couples with the ferromagnetic layer but does not change its orientation in an external magnetic field. Thus, higher fields are needed to change the orientation of the pinned ferromagnetic layer.

The stack of this sample is outlined in figure 4.11. Again silicon is used as substrate. The silicon is thermally oxidized so there is an insulator between bottom contact and substrate. The bottom contact consists of tantalum and ruthenium layers. On top of the ruthenium layer is an MnIr layer which is an antiferromagnet and needed to pin the bottom electrode. The bottom electrode itself consists of 3 nm CoFeB. Then there is a 1.5 nm thin MgO tunnel barrier. A 1.5 nm MgO barrier has also been investigated with the other stack. On top of the tunnel barrier is the second ferromagnetic layer. The alignments for these two CoFeB layers mainly influences the TMR and TMS ratio. Above is a permalloy layer and on the top of this ruthenium and tantalum. Once again a gold bond pad is used as the top contact.

### 4.5.1. TMR measurement

First, the TMR effect is measured again so that it is possible to estimate the quality of the barrier. The result is plotted in figure 4.12(a). Here, we do not have two peaks but a curve that is called minor loop. The reason for this behavior is that one layer is pinned and cannot change its direction if small magnetic fields are applied whereas the other layer is not pinned and can change its direction if a magnetic field higher than the coercive field is applied.



**Figure 4.11.:** Stack structure of the sample K120531a.

## 4. Experimental results

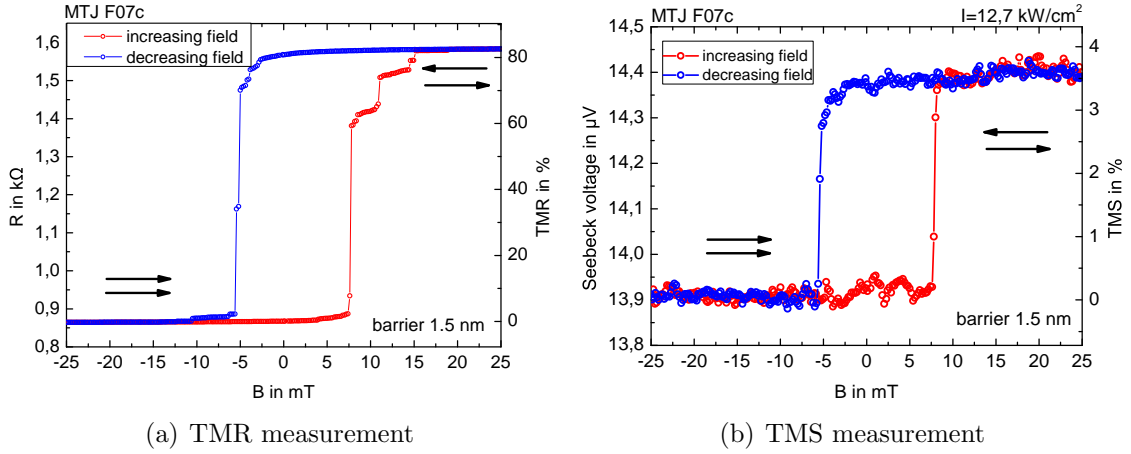


**Figure 4.12.:** TMS and TMR curves for the sample with exchange bias. The curves are called minor loops. Measurements with increasing and decreasing magnetic field are plotted in different colors. Arrows indicate the relative alignment of the magnetic layers.

The TMR effect is also plotted in figure 4.12(a) on the right axis. The maximum value of the effect is 80%. This is a relatively small effect for CoFeB/MgO junctions. But the switching behavior of the measured junction is good because there are sharp steps which means that the entire electrode switches at once (in contrast with many domains that all switch separately). However for  $B > 0$  domains can also be seen. The resistance of this sample (K120531a) is one order of magnitude higher as the resistance of the sample without exchange bias but with the same barrier thickness (vd120111-1.5, figure 4.4(c)). The reason is mainly that the area of the tunnel junction is bigger on the sample vd120111-1.5.

### 4.5.2. TMS measurement in detail

In the TMS measurement 4.12(b) the same switching behavior can be seen as in the TMR measurement. But here the effect is much smaller (about 3.5%). It has to be admitted that  $I = 12.7 \text{ kW/cm}^2$  is already the highest intensity applied to the sample because the laser was not well focused. The beam waist in these measurements was  $w = 23.2(5) \mu\text{m}$  which is twice as much as in the measurements of the previous section. Compared with the TMS measurement of the sample without exchange bias (figure 4.6(d)) the voltages are much higher and the TMS

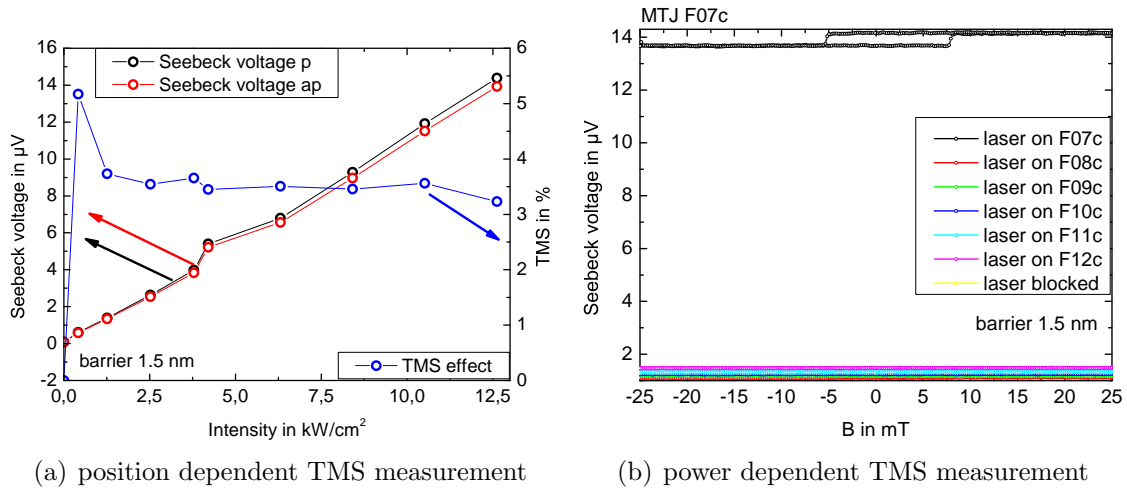


**Figure 4.13.:** TMS measurement as a function of the applied laser power and as a function of the heating position.

effect is higher for the same intensity, although the TMR effect is smaller.

### 4.5.3. TMS - position dependent measurement

In figure 4.13(a) the TMS effect is plotted for different laser intensities. As observed before the Seebeck voltage increases with increasing laser intensity. For this measurement the increase is linear. The TMS effect on the other hand does not increase linearly but remains constant between 3% and 4%. Just for the smallest applied intensity the effect is at around 5%. When the laser is blocked, no effect can be observed.

In these measurements the effect is always positive. This is in contrast to the measurements performed on the sample vd120111-1.5 which has the same barrier thickness (figure 4.6(d)). In that sample the TMS effect was always negative. A reason for this behavior can be that the antiferromagnetic exchange layer has an influence on this measurement. Therefore it may be better to use systems as simple as possible to reduce voltages originating from other layers and interfaces.

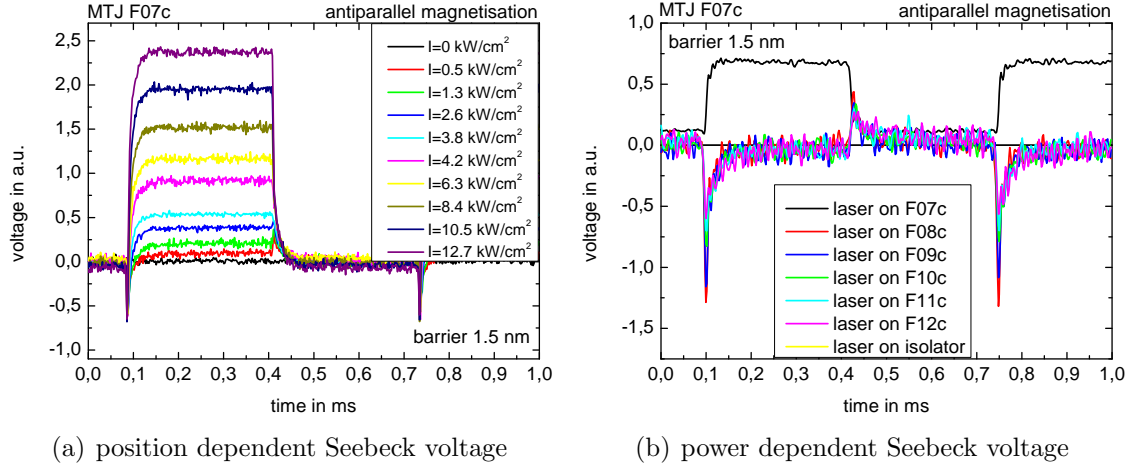


**Figure 4.14.:** Time resolved voltage signal measured at the top and bottom contacts of the sample. At about  $t = 0.1$  ms the laser starts heating the sample. At  $t = 0.4$  ms the laser is switched off.

#### 4.5.4. TMS - power dependent measurement

In figure 4.13(b) it can be seen clearly that the Seebeck voltage detected by the lock-in amplifier decreases by one order of magnitude if the sample is heated somewhere else. Nevertheless there is still a Seebeck voltage. The position dependent measurement with the sample vd120111-1.5 (figure 4.9(c)) revealed that the thermo voltage is smallest if the laser heats exactly on the junction. This result cannot be confirmed here. So there must be additional effects and the voltage does not just depend on the barrier thickness. The magneto-Seebeck effect does not just depend on the barrier thickness either because it differs in both measurements. The different layers and the exact composition of the junction and the MgO barrier have a significant influence.

#### 4.5.5. Time dependent Seebeck voltage.

Figure 4.14(a) shows the time dependent Seebeck voltage in the antiparallel state. Again there is a rectangular signal. The amplitude of this signal increases with increasing laser power. Additionally, there are peaks. These peaks do not change for higher laser powers. Compared with the sample vd120111-1.5 the peaks are much smaller in relation to the rectangular signal.

Also the position dependence of the Seebeck voltage differs for the samples vd1201111-1.5 and K120531a. The position dependence for the sample K120531a is plotted in figure 4.14(b). Only in the case that the laser directly heats the junction, there is a rectangular signal. In all other cases only peaks followed by an exponential decay of the Seebeck voltage are visible.

#### 4.5.6. MTJs as capacitors

As explained for the samples vd120111-x it may be possible that capacitive effects are responsible for the exponential decay process. Again exponential functions are fitted to all measured decaying processes. Thus it is possible to determine the time constant. This time constant is used to calculate the capacitance (equation (4.3)) as a function of the laser heating position. The results are plotted in figure 4.15. For increasing distances the time constant gets larger and thus the decay is slower. Because the time constant and the capacitance are proportional, the capacitance grows also.

This cannot be explained in a simple model of a parallel plate capacitor because a higher capacitance would mean a bigger area of the plates if the distance between the plates is considered as constant. It could rather be that mutual capacitances are important.

Figure 4.11 shows that there are two insulating layers: MgO between the two ferromagnetic layers and silicon oxide between substrate and bottom contact. With these two insulators three capacitors can be constructed. The dielectric of the first capacitor is just the MgO layer, the dielectric of the second capacitor is just the

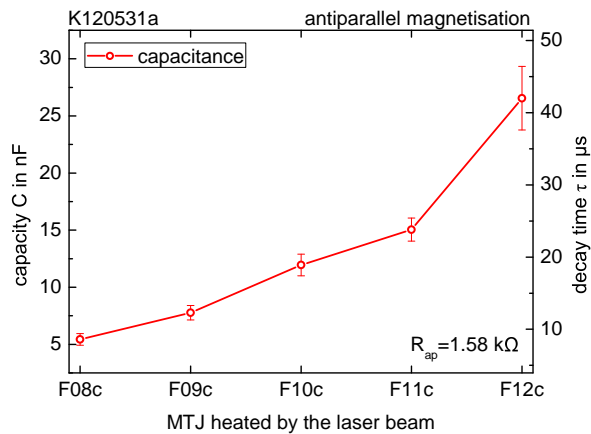


**Figure 4.15.:** The right axis shows the decay time as a function of the laser spot position. On the left axis the associated capacitance is plotted.

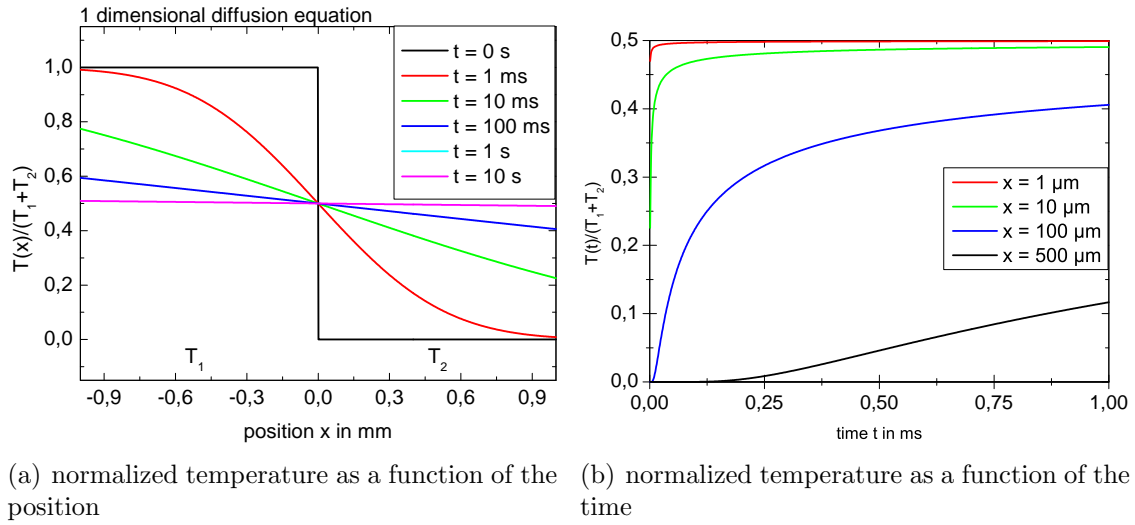


**Figure 4.16.:** Solution of the 1-dimensional heat diffusion equation for different times and positions.

silicon oxide layer and the dielectric of the third capacitor are both insulators plus the layers between this two insulators. If now one capacitor is loaded, for example the capacitor with MgO as dielectric, the other capacitors are loaded, too. This of course influences also the other MTJs, especially the contacted MTJ. So the substrate may play an important role by analyzing the peaks. If the substrate would be an insulator also, some mutual capacitances can be eliminated.

#### 4.5.7. Thermal diffusion in silicon

Another possibility to explain the peaks in the oscilloscope traces (figure 4.14(b)) is the thermal diffusivity. If the laser heats the tunnel junction, the heat diffuses into the substrate. It is possible that the substrate conducts the heat and resulting in a temperature gradient in the substrate. This would induce thermo-voltages that are related to the peaks.

A simple 1-dimensional model is used to estimate the time constants of the heat diffusion processes. In this model two areas with different temperatures at the time  $t = 0$  are considered. These areas can exchange heat. So the boundary conditions

are:

$$T(x, t = 0) = \begin{cases} T_1 & \text{if } x < 0, \\ T_2 & \text{if } x > 0. \end{cases} \quad (4.5)$$

This system can be described with the diffusion equation:

$$\frac{\partial T}{\partial t} = D \frac{\partial^2 T}{\partial x^2}. \quad (4.6)$$

Here  $D$  is the diffusion constant. A solution for the one dimensional heat diffusion equation with the boundary condition of different temperatures at different areas is given by:

$$T(x) = \frac{T_2 + T_1}{2} \left( 1 - \operatorname{erf} \left( \frac{x}{\sqrt{4Dt}} \right) \right). \quad (4.7)$$

For silicon the diffusion constant is  $D = 8.8 \cdot 10^{-5} \text{ m}^2/\text{s}$  [6, p. 168]. The solution of the heat equation is plotted in figure 4.16(a) as a function of the position for different times and in figure 4.16(b) as a function of the time for different positions. In the position dependent plot (figure 4.16(a)) one can see that both areas have a different temperature for  $t = 0$ . After some time there is a heat flux from the hotter region to the colder region. An equilibrium state is reached when both areas have almost the same temperature. On a distance of 1 mm an equilibrium state is reached after 1 s. In this simple model no heating process is considered. For a more realistic model with heat source and heat sink a temperature gradient would be expected in equilibrium.

Figure 4.16(b) shows the temperature as a function of the time for different positions. An equilibrium state is reached for  $T(x, t)/(T_1 + T_2) = 0.5$ . So the general trend is that it takes more time to reach an equilibrium if the distance gets bigger. By considering the stack in figure 4.11 it is possible to see that the diffusion distance from the gold bond pad to the tunnel junction is on the order of nanometers. So on this distances the heat is transferred very fast. On the other hand, if diffusion in the substrate is considered, the distances would be much bigger (magnitude of micrometers). Figure 4.16(b) shows that it needs time on the scale of milliseconds to reach the equilibrium.

The laser used as heat source in the experiment is modulated with 1.5 kHz. So the duration of one heat period is just  $t = 0.67$  ms. This is the same time scale as the diffusion processes on the scale of micrometers. The oscilloscope traces (figure 4.14(a)) on the other hand show that the peaks appear immediately after the laser is switched on (in the time scale of modulation). So diffusion processes in silicon are unlikely because they are too slow.

## 4.6. Thermal simulation

To calculate the Seebeck coefficients with the measured values of the Seebeck voltage, the temperature gradient is needed. Therefore, thermal simulations have been made for the sample vd120111-2.1. The heating was implemented with a Gaussian function of the form

$$p = \frac{\alpha_{\text{abs}}}{\lambda} e^{\frac{z}{\lambda}} \frac{2P}{\pi\omega^2} e^{-\frac{2r^2}{\omega^2}}, \quad (4.8)$$

because in the experiment also a beam with Gaussian profile is considered for heating.  $p$  is the power density (power per volume),  $\alpha$  the absorption coefficient and  $\lambda$  the optical penetration depth. As a heat sink the bottom of the substrate is set to room temperature.

The simulation is time independent. This means that the equilibrium state is simulated. For the calculation of the Seebeck coefficients only the temperature gradient along the tunnel junction is important. But the distance between tunnel junction and gold surface is just in the order of 100 nm. From

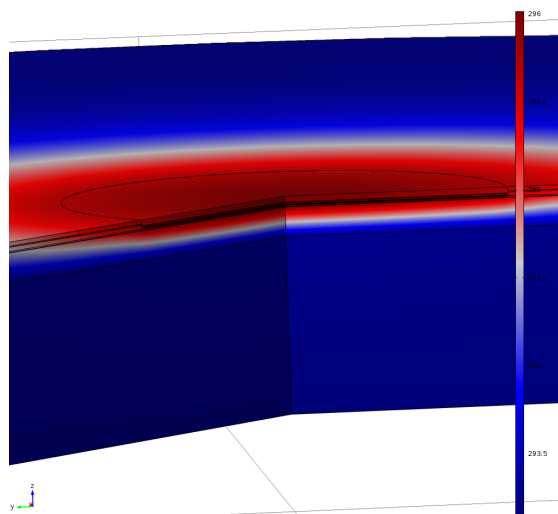


**Figure 4.17.:** Temperature distribution along the magnetic tunnel junction. The junction can be found in the center of the picture.

section 4.5.7 it is known that heat transport is fast on this short distances. So the

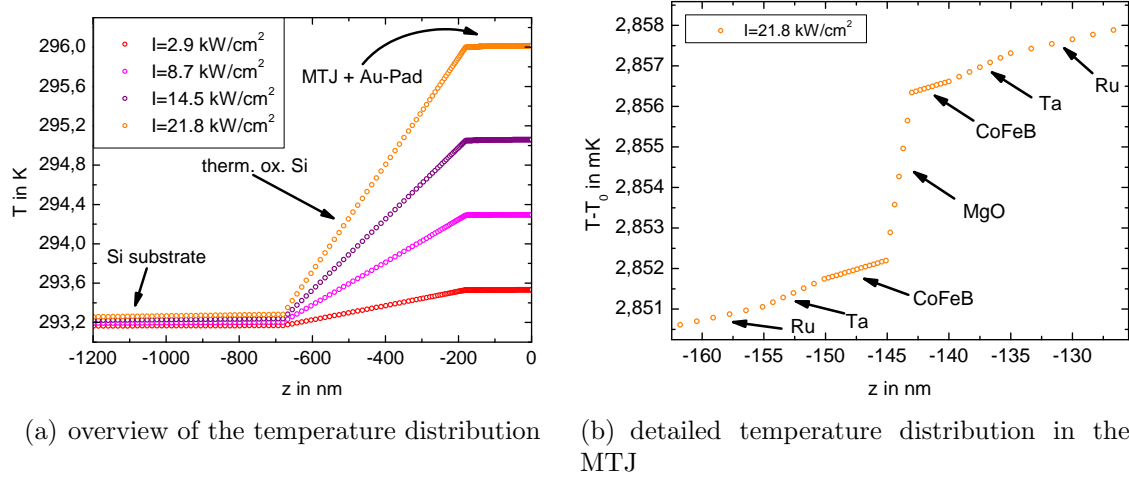


**Figure 4.18.:** Temperature distribution in the tunnel junction. Different layers can be distinguished.

steady state is reached immediately for this system on the modulation timescale and simulation of the equilibrium state is justified.

The result of the simulation is plotted in figure 4.17. The junction is in the center of the picture. To simplify the simulation, a system with radial symmetry was considered. The red areas in figure 4.17 indicate hot regions and the blue areas cold regions (room temperature). So it is obvious that the temperature at the top is high and then falls quickly. In the top part the temperature gradient is also higher.

For a more detailed analysis the heat profile is plotted in figure 4.18 (temperature gradient as a function of the penetration depth in the center of the junction). In the overview one can see that the heat drop in the whole MTJ is quite low but there is a huge temperature gradient in the silicon oxide insulator. In the silicon the temperature is nearly constant at room temperature  $T_0 = 293.15 \text{ K}$ , thus there is just a low temperature gradient.

Figure 4.18(b) shows the temperature gradient in more detail. Arrows indicate the different layers. In the MgO and CoFeB layers one can see more data points. The reason is that a finer mesh was chosen in the simulation for this area to get a higher precision. Because MgO is not only an electrical insulator but also a thermal insulator, the temperature gradient is high along the 2.1 nm thick MgO layer.

Next, the temperature gradient along the tunnel junction has to be estimated as a function of the applied laser power. The temperature difference between the top of

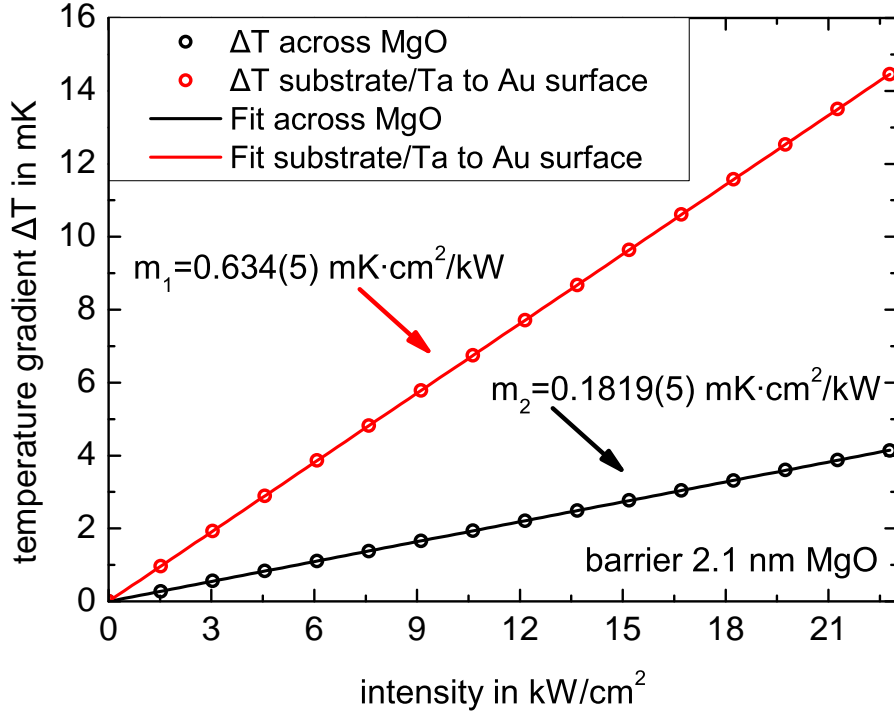


**Figure 4.19.:** Temperature gradient along the MTJ as a function of the applied power.

the MgO layer and the bottom of the MgO layer was taken as lower limit for the temperature gradient and the temperature gradient between the Au layer ( $z = 0$ ) and the top of the  $\text{SiO}_x$  was determined as an upper limit.

Both temperature differences are plotted in figure 4.19. They seem to depend linear on the applied power. So a linear function was fitted. To calculate the temperature gradient the following equation can be used:

$$\Delta T = I \cdot m_{1,2} ,$$

$$m_1 = 0.634(5) \text{mK} \cdot \text{cm}^2 / \text{kW} , \quad m_2 = 0.1819(5) \text{mK} \cdot \text{cm}^2 / \text{kW} .$$

The error is given by the fit. With these constants one can obtain the Seebeck coefficients plotted in figure 4.20. The Seebeck coefficients are represented as a function of the intensity and as a function of the temperature. To calculate the upper limit of the Seebeck coefficients the temperature gradient across the MgO

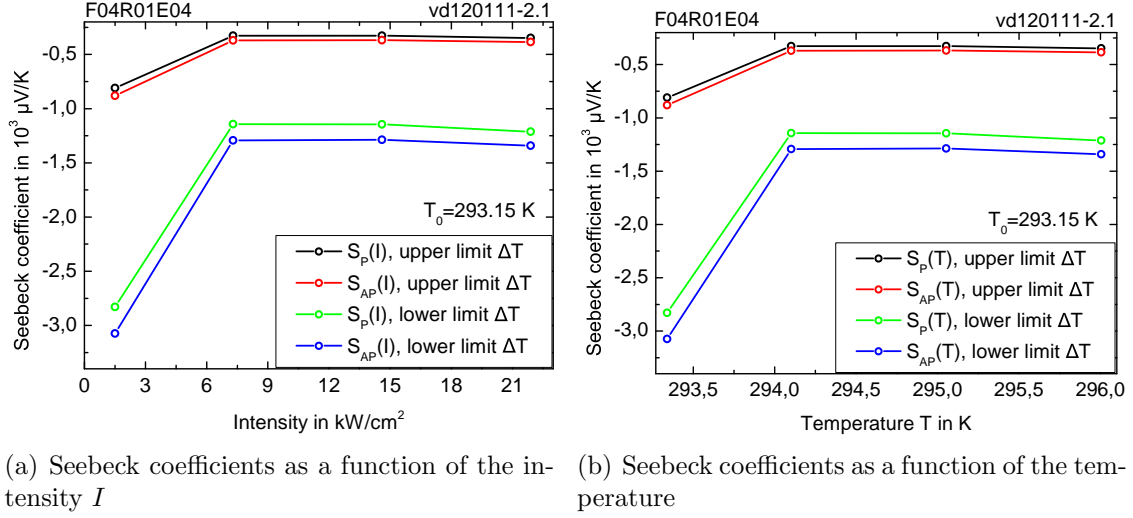


**Figure 4.20.:** Calculated Seebeck coefficients for the sample vd120111-2.1.

barrier is used and for the lower limit the Seebeck coefficients are calculated with the temperature gradient between substrate/Ta interface and Au surface. Figure 4.20 shows that the calculated Seebeck coefficients are quite low, especially for the smallest intensity of  $I = 1.5 \text{ kW/cm}^2$ . For increasing temperature and intensity, the absolute value of the Seebeck coefficients are smaller and then remain constant. The Seebeck coefficients are always negative. This can be estimated because the oscilloscope traces (figure 4.14(a)) indicate that the voltage is always positive. If the Seebeck coefficients are compared to the Seebeck voltage (figure 4.6(b)) complementary properties can be seen. The Seebeck voltage increases with the laser power and thus with the intensity, while the Seebeck coefficients remain constant for higher intensities above  $I = 7 \text{ kW/cm}^2$ . Of course the magneto-Seebeck effect does not change depending on the use of the Seebeck coefficients or the Seebeck voltage.

The Seebeck coefficients as a function of the temperature (figure 4.20(b)) can be compared to theoretical results (figure 2.6) because a barrier thickness of 2.1 nm correspond to 10 mono layers of MgO. As well the theoretical values for the Seebeck coefficients as the measured values are always negative. A result of the theoretical simulations is that the Seebeck coefficient for antiparallel magnetization  $S_{AP}$  are smaller as the Seebeck coefficients for parallel magnetization  $S_P$  and thus the Seebeck effect at room temperature is negative.

#### 4. *Experimental results*

---

However, in the measurements the magneto-Seebeck effect is always positive on the sample vd120111-2.1 and  $S_P$  is smaller than  $S_{AP}$ . The absolute values of the measured Seebeck coefficients are one order of magnitude higher than the calculated values.

# 5. Summary

## 5.1. Influence of the MgO barrier

Based on the results of this thesis, there is an indication that the MgO barrier has an influence on the magneto-Seebeck effect. For the layer of 2.1 nm the effect was always positive. The sample with 1.8 nm MgO barrier showed a sign change for an intensity of  $I = 2.3 \text{ kW/cm}^2$ . For the sample with 1.5 nm MgO barrier the effect was always negative. Nevertheless, the results for the sample vd120111-1.8 have to be considered carefully. The reason is that it was possible to observe an “TMS” like effect also when the laser was blocked. The origin of this parasitic signal is not understood, but crosstalk in ground loops with the same frequency as the reference signal for the lock-in amplifier probably plays a role.

The oscilloscope traces showed a peak and a plateau level. The plateaus belong to the Seebeck signal. In order to explain the peaks, a simple capacitor model and thermal diffusion was considered. However, thermal diffusion is too slow to explain the peaks which appear immediately after the laser was switched on (in ms time scale). The capacitance of a tunnel junction on the other hand is too small to explain the exponential decay of the voltage signals after the peak arises. Therefore mutual capacitances in the sample and substrate can play a role. To prevent this, an insulating substrate could be used in future experiments.

Also a sample with exchange bias and 1.5 nm MgO barrier was considered. In contrast to the sample with the same MgO barrier thickness but without exchange bias, an always positive effect was observed. This shows that the exact composition of the MgO and CoFeB at the boundaries is very important for the TMS effect. This assumption is confirmed by theoretical calculation (figure 2.6).

To calculate the Seebeck coefficients a temperature gradient is needed. This temperature gradient can be estimated with simulations. The simulations are time

independent because considerations with the 1 dimensional heat equation and earlier time dependent simulations show that the equilibrium is reached very fast on short distances like in this problem.

The resulting Seebeck coefficients are very high. So the upper limit for the temperature gradient seems more realistic. Nevertheless Seebeck coefficients in the order of 1000  $\mu\text{V}/\text{K}$  seems too high. A reason for these high values could be that the measured voltages are too high because there are additional voltages. The origin of these additional voltages are some noise sources that could not be eliminated yet and thermal voltages from other layers and interfaces.

## 5.2. Outlook

To estimate the influence of the substrate, the same tunnel junctions should be grown on a different substrate like MgO. MgO is an insulator and thus one would eliminate mutual capacitances. The peaks in the oscilloscope traces should then vanish.

The results show that the exact layer composition has a strong influence on the magneto-Seebeck effect. If the composition is varied systematically, it could be possible to describe this dependence systematically.

With reflectivity measurements it is possible to measure the temperature at the surface of the layers. This could be used to verify the simulations.

In this thesis the Seebeck voltage is always measured with a lock-in amplifier. Another possibility is to use a nano voltmeter. In that case modulation is not necessary and therefore, only the static temperature gradient is measured. Consequently, there would not be any peaks because they decay exponentially.

# A. Laser intensity

## A.1. Determining the beam waist

The beam waist measurement is necessary to calculate the intensity of the laser (power per area). To determine this parameter, the *knife edge method* is used. In this method the sample is moved perpendicular to the laser beam in a way that the laser spot crosses a boundary between parts with different reflectivity (figure A.1). The power of the reflected light is measured. It is important that there is a sharp transition between the areas with different reflectivity and that the boundary is perpendicular to the direction of movement. For all measurements it is assumed that our laser spot has a Gaussian profile. So the intensity of the incoming beam can be written as



**Figure A.1.:** Beam is moved along a sharp edge to determine the beamwaist.

$$I_{\text{in}}(x,y) = I_0 \cdot e^{-\frac{2x^2}{\omega_x^2}} \cdot e^{-\frac{2y^2}{\omega_y^2}}. \quad (\text{A.1})$$

For that profile the  $1/e^2$  radius in  $x$ -direction ( $y = 0$ ) is given by  $\omega_x$ . So  $\omega_x$  is the beam waist, which should be measured. If the laser spot hits a part of the sample with areas of different reflectivity like in figure A.1, the power of the reflected light can be calculated with:

$$P = \int_{-\infty}^{\infty} dx \int_{-\infty}^{\infty} dy I_{\text{out}}(x,y). \quad (\text{A.2})$$

$I_{\text{out}}$  depends on the position of the laser spot. Because both areas in figure A.1 have a different reflectivity,  $I_{\text{out}}$  is given by

$$I_{\text{out}}(x,y) = \begin{cases} I_2 \cdot e^{-\frac{2x^2}{\omega_x^2}} \cdot e^{-\frac{2y^2}{\omega_y^2}} & \text{if } x < x_0 , \\ I_1 \cdot e^{-\frac{2x^2}{\omega_x^2}} \cdot e^{-\frac{2y^2}{\omega_y^2}} & \text{if } x > x_0 . \end{cases} \quad (\text{A.3})$$

Here  $x_0$  is the position of the boundary between the two areas with different reflectivity. If the power of the reflected beam is calculated with this intensity, one gets two convolution integrals

$$P = \int_{-\infty}^{\infty} dx \int_{-\infty}^{\infty} dy I_2 \cdot e^{-\frac{2x^2}{\omega_x^2}} \cdot e^{-\frac{2y^2}{\omega_y^2}} \cdot \vartheta(x_0 - x) , \\ + \int_{-\infty}^{\infty} dx \int_{-\infty}^{\infty} dy I_1 \cdot e^{-\frac{2x^2}{\omega_x^2}} \cdot e^{-\frac{2y^2}{\omega_y^2}} \cdot \vartheta(x - x_0) . \quad (\text{A.4})$$

Thus the power is a convolution of the Gaussian beam with the Heaviside step function. The integration over  $y$  can be taken out easily because it is a Gauss integral. The integration over  $x$  is divided in two parts for both integrals:

$$P = I_2 \cdot \sqrt{\frac{\pi}{2}} \cdot \omega_y \left\{ \int_{-\infty}^0 dx e^{-\frac{2x^2}{\omega_x^2}} + \int_0^x dx e^{-\frac{2x^2}{\omega_x^2}} \right\} \\ + I_1 \cdot \sqrt{\frac{\pi}{2}} \cdot \omega_y \left\{ \int_x^0 dx e^{-\frac{2x^2}{\omega_x^2}} + \int_0^{\infty} dx e^{-\frac{2x^2}{\omega_x^2}} \right\} . \quad (\text{A.5})$$

Again two of these four integrals can be taken out easily because they are Gaussian like. For the other two integrals the substitution  $t = \frac{\sqrt{2}x}{\omega_x}$  is used. So the limits of the two intervals have to be changed.

$$P = I_2 \cdot \sqrt{\frac{\pi}{2}} \cdot \omega_y \left\{ \frac{1}{2} \sqrt{\frac{\pi}{2}} \omega_x + \frac{\omega_x}{\sqrt{2}} \int_0^{\frac{\sqrt{2}x}{\omega_x}} dt e^{-t^2} \right\} \\ + I_1 \cdot \sqrt{\frac{\pi}{2}} \cdot \omega_y \left\{ -\frac{\omega_x}{\sqrt{2}} \int_0^{\frac{\sqrt{2}x}{\omega_x}} dt e^{-t^2} + \frac{1}{2} \sqrt{\frac{\pi}{2}} \omega_x \right\} . \quad (\text{A.6})$$

This expression can be simplified if the definition for the error function is used. To take a possible translation in  $x$  direction into account,  $x$  is substituted by  $x - x_0$ :

$$P = \frac{\pi}{4} \omega_x \omega_y \left\{ (I_2 + I_1) + (I_2 - I_1) \cdot \operatorname{erf} \left[ \frac{\sqrt{2}(x - x_0)}{\omega_x} \right] \right\}. \quad (\text{A.7})$$

As mentioned above,  $\omega_x$  is the  $1/e^2$  radius in  $x$ -direction and therefore the beam waist. To determine the beam waist, the power is measured position dependent. After that, the error function can be fitted. Here it is important to remember that the error function has just 4 degrees of freedom: translation in  $x$  and  $y$  direction, amplitude and slope. The factor  $\omega_y$  can not be determined in this measurement because the sample is just moved in  $x$  direction. But for an ideal Gaussian beam, the beam waist should not depend on the direction (radial symmetry). Therefore  $\omega_x = \omega_y$  is valid.

Additionally the shape of the curve is determined by  $\omega_x$  alone. The variables  $I_1$ ,  $I_2$  and  $x_0$  just stretch the curve or translate it. Thus the multiplication with  $\omega_x$  is not important for the fit. If one is only interested in the beam waist, the pre-factor can be set equal to one. Because of the missing pre-factor, the intensities are not normalized anymore. Thus they can be replaced by other constants. Consequently one

$$\Delta T = I \cdot m_{1,2}, \quad m_1 = 0.634(5) \text{mK} \cdot \text{cm}^2/\text{kW}, \quad m_2 = 0.1819(5) \text{mK} \cdot \text{cm}^2/\text{kW}.$$

would get the following fit function:

$$P = a + b \cdot \operatorname{erf} \left( \frac{\sqrt{2}(x - x_0)}{\omega_x} \right). \quad (\text{A.8})$$

$a$  and  $b$  are some pre factors. All degrees of freedom are minded because there are four free parameters. If the intensities of the reflected beam are important also, equation (3.26) must be used. But because equation (A.8) is more simple, it can be fitted easier.

## A.2. Calculating the intensity

Because the beam waist is known, it is possible to calculate the average intensity of the Gaussian beam by dividing the power exposed in the  $1/e^2$  radius with the  $1/e^2$  area. Unfortunately in the experiment only the whole power of the beam is measured with a power meter. Therefore the power in the  $1/e^2$  radius has to be calculated as a function of the overall beam power.

The overall beam power is simply an integral over the input intensity  $I_{\text{in}}$  (equation (A.1)):

$$P_{\text{in}} = \int_{-\infty}^{\infty} dx \int_{-\infty}^{\infty} dy \ I_{\text{in}}(x,y) = \frac{\pi}{2} I_0 \omega_x \omega_y .$$

To calculate the power exposed in the  $1/e^2$  area  $P_{\text{avg}}$ , the limits of the integral have to be modified:

$$P_{\text{avg}} = \int_{-\omega_x}^{\omega_x} dx \int_{-\omega_y}^{\omega_y} dy \ \underbrace{I_0 \cdot e^{-\frac{2x^2}{\omega_x^2}} \cdot e^{-\frac{2y^2}{\omega_y^2}}}_{I_{\text{in}}} . \quad (\text{A.9})$$

The idea is again to rewrite these integrals as error functions. Therefore the radial symmetry is used. Additionally the substitutions  $t = \frac{\sqrt{2}x}{\omega_x}$  and  $u = \frac{\sqrt{2}y}{\omega_y}$  have to be done:

$$P_{\text{avg}} = 2I_0 \omega_x \omega_y \underbrace{\int_0^{\sqrt{2}} e^{-t^2} dt}_{\text{erf}[\sqrt{2}]} \underbrace{\int_0^{\sqrt{2}} e^{-u^2} du}_{\text{erf}[\sqrt{2}]} . \quad (\text{A.10})$$

This result can be compared to the overall power  $P_{\text{in}}$ , which lead to:

$$P_{\text{avg}} = P_{\text{in}} \cdot \underbrace{\left( \text{erf} \left[ \sqrt{2} \right] \right)^2}_{0.9111} . \quad (\text{A.11})$$

So 91.11% of the laser power is emitted in the  $1/e^2$  area. Therefore the intensity of the laser in this area is given by:

$$I_{\text{avg}} = \frac{0.9111 \cdot P_{\text{in}}}{\pi \cdot \omega_x^2} . \quad (\text{A.12})$$

# Bibliography

- [1] Blügel, Bürgler, Morgenstern, Schneider, Waser, and Rainer. *Spintronics - From GMR to Quantum Information*. Forschungszentrum Jülich GmbH Institut für Festkörperforschung, 2009. ISBN 978-3-89336-559-3.
- [2] W. H. Butler, X.-G. Zhang, T. C. Schulthess, and J. M. MacLaren. Spin-dependent tunneling conductance of Fe|MgO|Fe sandwiches. *Phys. Rev. B*, 63:054416, Jan 2001. doi: 10.1103/PhysRevB.63.054416. URL <http://link.aps.org/doi/10.1103/PhysRevB.63.054416>.
- [3] H.B. Callen. *Thermodynamics and an introduction to thermostatistics*. Wiley, 1985. ISBN 9780471862567.
- [4] Michael Czerner and Christian Heiliger. Influence of interface termination on the magneto-seebeck effect in MgO based tunnel junctions. *Journal of Applied Physics*, 111(7):07C511, 2012. doi: 10.1063/1.3675987. URL <http://link.aip.org/link/?JAP/111/07C511/1>.
- [5] FEMTO Messtechnik GmbH. DPLVA-100-F-S. *Variable Gain Low Frequency Voltage Amplifier*, 2012.
- [6] R. Hull and INSPEC (Information Service). *Properties of Crystalline Silicon*. EMIS Datareviews Series. INSPEC, The Institution of Electrical Engineers, 1999. ISBN 9780852969335.
- [7] J. B. Johnson. Thermal agitation of electricity in conductors. *Phys. Rev.*, 32: 97–109, Jul 1928. doi: 10.1103/PhysRev.32.97. URL <http://link.aps.org/doi/10.1103/PhysRev.32.97>.
- [8] M. Julliere. Tunneling between ferromagnetic films. *Physics Letters A*, 54(3):225 – 226, 1975. ISSN 0375-9601. doi: 10.1016/0375-9601(75)

- 90174-7. URL <http://www.sciencedirect.com/science/article/pii/S0375960175901747>.
- [9] Jagadeesh S. Moodera and George Mathon. Spin polarized tunneling in ferromagnetic junctions. *Journal of Magnetism and Magnetic Materials*, 200(1–3):248 – 273, 1999. ISSN 0304-8853. doi: 10.1016/S0304-8853(99)00515-6. URL <http://www.sciencedirect.com/science/article/pii/S0304885399005156>.
- [10] R. Morrison. *Grounding and shielding techniques in instrumentation*. Wiley-Interscience Publication. Wiley, 1986. ISBN 9780471838050.
- [11] John G. Simmons. Generalized formula for the electric tunnel effect between similar electrodes separated by a thin insulating film. *Journal of Applied Physics*, 34(6):1793–1803, 1963. doi: 10.1063/1.1702682. URL <http://link.aip.org/link/?JAP/34/1793/1>.
- [12] Dicing Systems. KS 4500 series manual wire bonders. *Operation and Maintenance Manual*, 2002.
- [13] Stanford Research Systems. Model SR830 DSP lock-in amplifier. *Operating Manual and Programming Reference*, 2011.
- [14] P. M. Tedrow and R. Meservey. Spin-dependent tunneling into ferromagnetic nickel. *Phys. Rev. Lett.*, 26:192–195, Jan 1971. doi: 10.1103/PhysRevLett.26.192. URL <http://link.aps.org/doi/10.1103/PhysRevLett.26.192>.
- [15] V.K. Thankappan. *Quantum Mechanics*. J. Wiley, 1993. ISBN 9788122405262.
- [16] Marvin Walter, Jakob Walowski, Vladyslav Zbarsky, Markus Muenzenberg, Markus Schaefer, Daniel Ebke, Guenter Reiss, Andy Thomas, Patrick Peretzki, Michael Seibt, Jagadeesh S. Moodera, Michael Czerner, Michael Bachmann, and Christian Heiliger. Seebeck effect in magnetic tunnel junctions. *NATURE MATERIALS*, 10(10):742–746, OCT 2011. ISSN 1476-1122. doi: {10.1038/NMAT3076}.

# Acknowledgment

First I want to thank Marvin Walter. He mainly supported me in the laboratory and by writing my bachelor thesis. I learned a lot while working together with Marvin and had a lot of fun.

Further I want to thank Prof. Dr. Markus Münzenberg for supervising my bachelor thesis. Whenever new “challenges” occurred (like grounding problems) it was possible to discuss them with Markus. My thanks goes also to Prof. Dr. Claus Ropers for surveying this work.

Finally I give my thanks to the whole “spin group” for a good working climate, a pleasant time and unforgettable moments like having “Mettfrühstück” together.

**Erklärung** nach §13(8) der Prüfungsordnung für den Bachelor-Studiengang Physik und den Master-Studiengang Physik an der Universität Göttingen:

Hiermit erkläre ich, dass ich diese Abschlussarbeit selbständig verfasst habe, keine anderen als die angegebenen Quellen und Hilfsmittel benutzt habe und alle Stellen, die wörtlich oder sinngemäß aus veröffentlichten Schriften entnommen wurden, als solche kenntlich gemacht habe.

Darüberhinaus erkläre ich, dass diese Abschlussarbeit nicht, auch nicht auszugsweise, im Rahmen einer nichtbestanden Prüfung an dieser oder einer anderen Hochschule eingereicht wurde.

Göttingen, den 31. Juli 2012

(Niklas Roschewsky)